A&A 432, 1033–1047 (2005)
DOI: 10.1051/0004-6361:20041102

Astronomy & Astrophysics

The kinetic effects of electron beam precipitation and resulting hard X-ray intensity in solar flares⋆

V. V. Zharkova and M. Gordovskyy

Cybernetics and Virtual Systems Department, University of Bradford, Bradford BD7 1DP, UK
e-mail: m.gordovskyy@bradford.ac.uk

Received 16 April 2004 / Accepted 25 October 2004

Abstract. The numerical solutions of the time-dependent kinetic Fokker-Planck equation are presented for fast electrons injected from the solar corona into a flaring atmosphere and precipitating with energy and pitch-angle diffusion into a loop with a converging magnetic field. The electrons are assumed to lose their energy in Coulomb collisions with particles of the partially ionised ambient plasma and Ohmic heating owing to the electric field induced by the precipitating beam. The electric field induced by a precipitating electron beam is found to cause a return current beam, which comes back to the source in the corona with a wide pitch angle distribution. The return current is assumed to arise from the ambient plasma and from beam electrons scattered into negative pitch-angles. Energy and pitch-angle distributions of precipitating and return current electron beams at various atmospheric depths are presented along with the precipitating beam abundances, energy fluxes and resulting hard X-ray bremsstrahlung (photon) spectra for electron beams with power law energy spectra with spectral indices of 3, 5, 7 and initial energy fluxes of 10^8, 10^{10}, 10^{12} erg cm^{-2} s^{-1}. Energy distributions of the return current cover energies lower than 60 keV for weaker soft beams and increase to 65 keV for moderate soft beams, or to 70–75 keV for more intense and hard beams. The maxima are at 30 keV for weaker soft beams and are shifted towards higher energies, up to 50 keV, for harder and more intense beams.

As a result, the photon spectra of hard X-ray emission emitted from a flaring atmosphere are found to have a broken power-law (elbow-type) shape with a higher energy part retaining the spectral index $\delta_{\rm high}$ associated with the electron beam's initial index and varying slightly with the beam parameters. However, the lower energy part of the X-ray photon spectra shows a much smaller increase or even a substantial decrease of its spectral index $\delta_{\rm low}$ for more intense or harder beams. These simulated broken power-law photon spectra produced by precipitating electron beams with a single spectral index agree reasonably well with the photon energy spectra from the flares of 20 and 23 July, 2002 observed by the RHESSI payload.

Key words. Sun: flares – Sun: particle emission – Sun: X-rays, gamma rays

1. Introduction

Recent progress in the simultaneous observations of solar flares in hard X-ray (HXR) and UV observations with RHESSI (Lin et al. 2003) and TRACE (Seaton et al. 2001) correlated with high-resolution ground-based observations in radio and optical ranges confirmed their close temporal correlation and the high likelyhood that they are produced by the same population of non-thermal electrons (Vilmer et al. 2002; Wilson & Holman 2003). At the same time, the sources of MW and HXR emission are often at different depths within a flaring atmosphere and have different locations of the flaring footpoints (Sui et al. 2002).

The lower energy cutoff of photon spectra was shown to change from 10–20 keV (Tindo et al. 1972) to 30 keV (Holman & Benka 1992) or even up to 40 keV (Holman et al. 2003). However, the most important effect confirmed by the high resolution RHESSI observations was an elbow-type X-ray photon spectrum with a broken power-law energy distribution in most flares being reported by Lin et al. (2003), Holman et al. (2003) with the lower energy part having the indices 1.5–2.5 lower than those of the higher energy parts with energies higher than 50 keV. The attempts to explain these elbow-type spectra by collisions of beam electrons with charged particles and neutral atoms of the ambient plasma with non-uniform "thick-target" ionisation without taking into account particle diffusion in energy (Brown 1971; Conway et al. 2003; Kontar et al. 2003) required distributions of density and ionisation degree with depth that are difficult to imagine in real flares. This approach made it possible to deduce the relationship between the spectral indices γ and δ of the injected electrons and the emitted HXR photons respectively as $\delta = \gamma + 1/2 + \alpha$ where α is a parameter which describes plasma inhomogeneity with $\alpha = 0$ if the target plasma density distribution is uniform. However, this "mean path" approach is not fully applicable to the footpoint emission caused by precipitating beam electrons in the

⋆ Figures 3–6 are only available in electronic form at http://www.edpsciences.org

very dense plasmas of the solar chromosphere. This requires a revision of the existing kinetic approaches to the interpretation of HXR emission from solar flares.

Energy diffusion due to pure Coulomb collisions of electrons injected from the top in the corona and precipitating downwards into the fully ionised ambient plasma was shown to affect significantly the precipitating beam energy and resulting photon spectra for fully ionised (Syrovatskii & Shmeleva 1972) and partially ionised plasma (Zharkova & Kobylinskii 1993) without any additional assumptions about the structure of the target. The HXR photon indices were found to increase by 1.5 over those of beam electrons (Syrovatsky & Shmeleva 1972) that complied with the relationship found by Brown (1972). However, the authors did not take into account pitch-angle diffusion, which can change significantly the resulting electron and photon spectra.

The pitch-angle and energy diffusion were considered in the solutions of a stationary Fokker-Planck equation for high-energy electrons injected into a cold hydrogen plasma confined in open and closed magnetic field structures (Leach & Petrosian 1981). The precipitating beams were found to have single-power-law energy and pitch-angle distributions, the latter becoming wider with increasing depth. The magnetic field convergence was found to significantly reduce the beam precipitation depth leading to electron trapping in the corona and, as a result, to stronger coronal HXR emission (McClements 1990, 1992a).

However, high-density electron beams precipitating into a flaring atmosphere are expected to induce an electric field, which gives rise to a return current from the ambient plasma and causes precipitating electrons to return to the source (Knight & Sturrock 1977; Shapiro & Knight 1978; Emslie 1980). Diakonov & Somov (1988) formulated the electron kinetic problem taking into account both Coulomb collisions and the return current and solved this problem analytically for pure Ohmic heating in a collisionless plasma. They concluded that the return current caused a significant decrease of the electron penetration depth and, hence, a decrease of the hard X-ray intensity in comparison with that for pure Coulomb collisions. However, the authors did not specify any numerical relationship between electron and photon spectral indices.

The kinetic problem including all three effects (collisions, magnetic field and return current) was formulated by McClements (1992b) as a time-dependent Fokker-Planck equation. Syniavskii & Zharkova (1994) solved this problem numerically for a stationary injection of beam electrons, but overestimated the contribution of the induced electric field by the assumption that at all depths it was constant and equal to the electric field at the injection point. This led to all the beam electrons with energies higher than ≤120 keV returning to the source in the corona. Later Zharkova et al. (1995) considered a similar time-dependent kinetic problem but with the induced electric field varying with depth according to precipitating beam distribution functions. This approach reduced the maximum energy of beam electrons returning to the source to 90–100 keV and explained a wide range of the variations in HXR polarisation magnitudes and directivities (see e.g. Leach & Petrosian 1983; Zhitnik et al. 1993; Zharkova et al. 1995).

Therefore, the induced electric field reduces the number of precipitating electrons, that can change the resulting hard X-ray photon spectra significantly. The motivation of the present paper is to extend the electron distributions obtained by Zharkova et al. (1995) for a wider range of injected beam parameters, taking into account the contributions to a return current of both the ambient plasma and beam electrons, to produce the resulting electron flux and photon energy spectra and their spectral indices and to compare them with those deduced from the RHESSI observations.

The kinetic problem for high-energy electrons precipitating from a source in the corona into a converging coronal loop with energy and pitch-angle diffusion in the presence of an induced electric field, the method of solutions and adopted parameters for injected beams and flaring atmospheres are described in Sect. 2. Depth, energy and pitch-angle variations of the electron distribution function, particle densities of the injected and returning beams with their energy fluxes, resulting HXR photon spectra and a comparison with the RHESSI photon spectra are discussed in Sect. 3, and the conclusions presented in Sect. 4.

2. The formulation of the problem

2.1. The electron distribution function

Let us consider the precipitation of an electron beam injected from the top in the corona at a depth $x_{\min}$ to the bottom $x_{\max}$ of a one dimensional flaring atmosphere with a temperature T, density n and ionisation degree X varying with precipitation depth. Beam electrons at the injection point have a power-law energy distribution in the range from $E_{\rm low}$ to $E_{\rm up}$ with spectral index γ, and a normal distribution of pitch-angles θ with a dispersion $\theta_{\max} - \theta_{\min}$. The injection is assumed to have a rectangular temporal profile, i.e. it switches on at 0 s, lasts for a time t_0 and then instantly switches off.

The electron beam precipitation can be described by a time-dependent distribution function $f = f(t, x, E, \theta)$ in a phase space of precipitation depth x, particle energy E and pitch-angle θ between the electron velocity vector and the magnetic field direction. The distribution function is normalised to the number of beam particles in a given range of energy and pitch-angle at a given depth with a scaling factor K as follows:

$$N_{\rm b}(t, x) \equiv K \int_0^{\infty} \int_{-1}^{1} f(t, x, E, \theta) \mathrm{d}E \, \mathrm{d}(\cos\theta), \quad (1)$$

where the factor K can be defined as described in Sect. 2.5.

2.2. The basic equations

During precipitation, beam electrons induce an electric field, which produces a return current from the ambient plasma and precipitating electrons coming back to the source. Therefore, there are two basic equations describing the problem: a kinetic one for beam electrons and the Ampere one for the neutralisation of electric currents from the direct and returning beams. In the kinetic equation we neglect wave-particle interaction for beam electrons since their energy exchange with plasma waves

was not found to contribute significantly to the energy balance of fast electrons; however, the ion-acoustic waves can be another factor contributing to the beam kinetics if the return current is strong (see e.g. Benz 2002, p. 116). Hence, there are the two channels of electron beam energy losses during their precipitation: Coulomb collisions with charged and neutral particles of the ambient plasma and Ohmic heating through energy and pitch-angle diffusion. In addition, pitch-angle deflection of beam electrons caused by a converging magnetic field is considered which, in fact, takes into account that some electrons escape from a magnetic trap into the loss-cone for a strongly converging field. With these assumptions a beam electron distribution function is governed by Landau (1937), or the Fokker-Planck equation, in the following form (Diakonov & Somov 1988; Zharkova et al. 1995):

$$\frac{\partial f}{\partial t} + \sqrt{\frac{2E}{m_\mathrm{e}}}\cos\theta\frac{\partial f}{\partial x} - \frac{e\mathcal{E}}{m_\mathrm{e}}\sqrt{2m_\mathrm{e}E}\cos\theta\frac{\partial f}{\partial E} - \frac{e\mathcal{E}}{m_\mathrm{e}}\sin^2\theta\sqrt{\frac{m_\mathrm{e}}{2E}}\frac{\partial f}{\partial\cos\theta} = \left(\frac{\partial f}{\partial t}\right)_\mathrm{coll} + \left(\frac{\partial f}{\partial t}\right)_\mathrm{magn} \quad (2)$$

where e and m_e are electron charge and mass, respectively. The first term on the left-hand side describes the distribution function variations with time, the second those with depth, the third and fourth reflect the energy losses and pitch-angle diffusion in the presence of the electric field $\mathcal{E}$. The two terms on the right-hand side $\left(\frac{\partial f}{\partial t}\right)_\mathrm{coll}$ and $\left(\frac{\partial f}{\partial t}\right)_\mathrm{magn}$ describe the particle energy and pitch angle diffusion caused by energy losses in collisions with the ambient plasma particles (collisional integral) and in a converging magnetic field, respectively.

The collisional integral is taken in the linearised form suggested by Diakonov & Somov (1988):

$$\left(\frac{\partial f}{\partial t}\right)_\mathrm{coll} = \frac{m_\mathrm{e}^2}{2\sqrt{2E}}\frac{\partial}{\partial E}\left(\frac{\nu(E)}{\sqrt{E}}\left(k_B T_\mathrm{e}\frac{\partial f}{\partial E} + f\right)\right) + \nu(E)\frac{\partial}{\partial\cos\theta}\left(\sin^2\theta\frac{\partial f}{\partial\cos\theta}\right). \quad (3)$$

Here k_B is the Boltzmann gas constant, T_e is the ambient plasma electron temperature and $\nu(E)$ is the frequency of collisions, which can be written as follows:

$$\nu(E) = \frac{k}{\sqrt{2m_\mathrm{e}}}\pi n(x)\lambda e^4 E^{-\frac{3}{2}} \quad (4)$$

where $n(x)$ is the ambient plasma density, λ is the Coulomb logarithm for electrons and the parameter k is taken in the form suggested by Emslie (1978):

$$k = 5X + \frac{(1-X)\lambda''}{\lambda'}.$$

Here λ' and λ'' are the Coulomb logarithms for protons and neutral particles of the ambient plasma, respectively.

The effect of a magnetic field convergence can be taken into account in the form suggested by McClements (1992a):

$$\left(\frac{\partial f}{\partial t}\right)_\mathrm{magn} = \sqrt{\frac{2E}{m_\mathrm{e}}}\frac{\sin^2\theta}{2}\frac{\partial\ln B(x)}{\partial x}\frac{\partial f}{\partial\cos\theta}, \quad (5)$$

where $B(x)$ is the longitudinal component of the magnetic induction at the given depth x.

The electric current carried by precipitating beam electrons can be determined as

$$j(x) = 2\pi e\int_0^\infty\int_{-1}^1 f(x,E,\theta)v_x\mathrm{d}E\,\mathrm{d}\cos\theta,$$

or, since $v_x = \sqrt{\frac{2E}{m_\mathrm{e}}}\cos\theta$, it can be rewritten as follows:

$$j(x) = 2\sqrt{2}\pi\frac{e}{\sqrt{m_\mathrm{e}}}\int_0^\infty\int_{-1}^1 f(x,E,\theta)\sqrt{E}\cos\theta\mathrm{d}E\,\mathrm{d}\cos\theta. \quad (6)$$

The electric current carried by precipitating electrons is assumed to be fully compensated by that carried by return current electrons. Hence, the return current electric field can be written as follows:

$$\mathcal{E} = \frac{j_{rc}(x)}{\sigma(x)} = \frac{j(x)}{\sigma(x)} = \frac{2\sqrt{2}\pi}{\sigma(x)}\frac{e}{\sqrt{m_\mathrm{e}}}\int_0^\infty\int_{-1}^1 f(x,E,\theta)\sqrt{E}\cos\theta\mathrm{d}E\,\mathrm{d}\cos\theta, \quad (7)$$

where $\sigma(x)$ is the ambient plasma classic conductivity (see e.g. Benz 2002, p. 216). Therefore, Eqs. (2), (3) and (5) define electron beam precipitation in the adopted model.

2.3. The dimensionless equations

In order to simplify Eq. (2) one can introduce new dimensionless variables as in Diakonov & Somov (1988). Let us describe the column density ξ as a function of the precipitation depth x as follows:

$$\xi = \int_0^x n(x)\mathrm{d}x. \quad (8)$$

Since the characteristic (average) energy of a beam is the lower energy cutoff E_low, the characteristic column density can be defined as $\xi_0 = \frac{E_\mathrm{low}^2}{2a}$, which is a column density where the electrons with energy E_low completely lose their energy. The collisional parameter a takes into account beam electron scattering on particles of the ambient plasma for a given ionisation degree X defined by Zharkova & Kobylinskii (1993):

$$a = 2\pi e^4\left[X\ln\frac{2Eb_0}{e^2} + X\ln\frac{2m_0Eb_0}{m_\mathrm{e}e^2} + (1-X)\ln\frac{2E}{1.105I_\mathrm{n}}\right], \quad (9)$$

where the terms on the right hand side are related to beam electron scattering on electrons (first), protons (second) and neutral hydrogen atoms (third). I_n is the full ionisation potential of a hydrogen atom, E is the electron energy, b_0 is the target distance, assumed to be equal to the Debye length, as follows (see e.g. Krall & Trivelpiece 1973):

$$b_0 = \sqrt{\frac{k_B T}{4\pi n e^2}}.$$

It can be seen that the parameter a depends directly on the ionisation degree only and varies logarithmically with the electron

energy and the ambient plasma temperature, and with density via the Debye length. For a typical electron energy ~100 keV and an ambient plasma density about 10^{11} cm^{-3} this parameter is equal to 2.7×10^{12} eV^2 cm^2 for the fully ionised plasma, decreasing to 2.3×10^{12} eV^2 cm^2 for the fully neutral ambient plasma.

From the definition of column density and kinetic energy E one can deduce a characteristic length $l_0 = \xi_0/n(\xi)$ and velocity $V_0 = \sqrt{\frac{2E_{\rm low}}{m_{\rm e}}}$, that define a characteristic time $t_0 = \frac{l_0}{V_0} = \frac{\sqrt{2m_{\rm e}}E_0^{\frac{3}{2}}}{2\pi e^4 n\lambda}$.

Therefore, the original variables can be referred to these characteristics, leading to a dimensionless depth $s = \xi/\xi_0$, energy $\eta = E/E_{\rm low}$, pitch-angle cosine $\mu = \cos\theta$ and time $\tau = t/t_0$. A dimensionless electric field ε can be measured in units of the Dreicer electric field $\varepsilon_0 = \mathcal{E}_{\rm D} = \frac{2\pi e^3 \lambda n(x)}{k_{\rm B}T_{\rm e}}$ giving $\varepsilon = \mathcal{E}/\mathcal{E}_{\rm D}$.

Hence, Eq. (2) can be re-written in dimensionless variables as follows:

$$\eta^{1.5}\frac{\partial f}{\partial \tau} + \mu\eta^2\frac{\partial f}{\partial s} - 2\varepsilon\mu\eta^2\frac{\partial f}{\partial \eta} - \varepsilon\eta\left(1-\mu^2\right)\frac{\partial f}{\partial \mu} = \frac{k}{2}\left[2\beta\eta\frac{\partial^2 f}{\partial \eta^2} + 2\eta\frac{\partial f}{\partial \eta} - 2\mu\frac{\partial f}{\partial \mu} + \left(1-\mu^2\right)\frac{\partial^2 f}{\partial \mu^2}\right] + \frac{\eta^2\left(1-\mu^2\right)}{2}\frac{\partial \ln B}{\partial s}\frac{\partial f}{\partial \mu}. \quad (10)$$

The parameter β defines the ratio of the average thermal to beam energies of the interacting electrons $\beta = \frac{k_{\rm B}T_{\rm e}}{E_{\rm low}}$ where $T_{\rm e}$ is the electron temperature of the ambient plasma. Normally, in the corona and chromosphere this parameter is very small, i.e. $\beta \approx 10^{-3}$–10^{-4} and in the first approach this term can be neglected.

The magnetic field in the flaring loop is assumed to grow exponentially with the column density, i.e. from $B(\xi_{\rm min})$ to $B(\xi_{\rm max}) = \alpha\, B(\xi_{\rm min})$ where α is the convergence constant, $\xi_{\rm min}$ is the column depth at injection and $\xi_{\rm max}$ the column depth at the bottom of the atmosphere. Hence, the magnetic field term can be rewritten in the following form:

$$B(\xi) = B(\xi_{\rm min})\alpha^{\frac{\xi-\xi_{\rm min}}{\xi_{\rm max}-\xi_{\rm min}}}, \quad (11)$$

and, therefore, the parameter describing convergence in Eq. (5) will be constant, and the coefficient defining the magnetic field convergence can be found from the formula:

$$\frac{{\rm d}\ln B(\xi)}{{\rm d}\xi} = \frac{\ln\alpha}{\xi_{\rm max}-\xi_{\rm min}}.$$

2.4. The initial and boundary conditions

In the present paper we consider the quasi-stationary kinetic problem: the steady-state solution of the Boltzmann kinetic Eq. (1) (or Eq. (10) in dimensionless form) is sought. Then, by varying the initial beam parameters (boundary condition at $\xi = \xi_{\rm min}$) we consider the beam variation with time and apply this to calculation of the HXR spectra. This approach is valid for time-scales longer than the beam decay time $\tau_{\rm dec}$, which is deduced below.

In order to make the problem self-consistent one needs to determine the initial and boundary conditions for an electron distribution function in the 4-variable phase space considered, with two independent variables (time and depth) and the other two dependent on the first two (energy and pitch-angle). Assuming that there are no beam electrons present in a flaring atmosphere prior to their injection, the initial condition at $t = 0$ has to define the initial beam injection from the top boundary as follows:

$$f(s > s_{\rm min}, \eta, \mu)\,|_{t=0} = 0;\;\; f(s = s_{\rm min}, \eta, \mu)\,|_{t=0} = f(s_{\rm min}, \eta, \mu), \quad (12)$$

which is supposed to hold for the injection time from 0 until t_0.

There are three variables: depth, energy and pitch-angle cosine, the lower and upper boundaries of which have to be defined. The boundary $\eta_{\rm min}$ is defined by the energy which is assumed to separate thermal and non-thermal electrons and that is accepted to be about 10–15 keV (Holman & Benka 1992), i.e. $\eta_{\rm min} = 1$. The boundary at $\eta = \eta_{\rm max}$ is defined by the upper energy cutoff at the injection $E_{\rm upp}$, chosen to be smaller than the relativistic limit ($E_{\rm upp} < 511$ keV), i.e. $\eta_{\rm max} = E_{\rm upp}/E_{\rm low}$. The boundary at $s = s_{\rm max}$ as well as the pitch-angle cosine boundaries $\mu_{\rm min} = -1$ and $\mu_{\rm max} = 1$ are chosen to be "free" boundaries, meaning that there are no dramatic changes in the distribution function or its derivatives when the particle passes through them, i.e.:

$$f(s_{\rm max}, \eta, \mu) = f(s_{\rm max} - {\rm d}s, \eta, \mu),$$

$$\left(\frac{{\rm d}f}{{\rm d}s}\right)_{(s=s_{\rm max})} = \left(\frac{{\rm d}f}{{\rm d}s}\right)_{s=s_{\rm max}-{\rm d}s},$$

which is valid also for pitch angle boundaries if $s_{\rm max}$ is replaced either with $\mu_{\rm min}$ or $\mu_{\rm max}$.

The distribution function at the top boundary $s = s_{\rm min}$ is defined by the initial energy – pitch-angle distribution of the injected beam. We assume that the injected beam has a power-law energy spectrum in the range $E_{\rm low}$ to $E_{\rm upp}$ with a spectral index γ and normal distribution of a pitch-angle cosine with a half-width dispersion $\Delta\mu = \mu_{\rm max0} - \mu_{\rm min0}$, where the subscripts max and min define the maximum and minimum pitch-angle cosine at injection. Therefore, the boundary condition at the upper boundary on depth $s = s_{\rm min}$ is defined by the formula:

$$f(s_{\rm min}, \eta, \mu) = \begin{cases} \eta^{-\gamma-0.5}\exp\left(-\left(\frac{\mu-1}{\Delta\mu}\right)^2\right) U(\tau), & 1 < \eta < \eta_{\rm max} \text{ and } \mu > 0 \\ 0, & \text{elsewhere} \end{cases}. \quad (13)$$

Here $U(\tau)$ is the temporal profile of the electron beam injection, which denotes the initial beam flux variations. If steady injection is considered, $\partial f/\partial t = 0$, then $U(\tau) =$ constant. Let us evaluate, if this is valid for the proposed model.

One can estimate the decay time for non-thermal electrons from the collision frequency discussed in Sect. 2.2 (Eq. (4)) as follows:

$$\tau_{\rm dec} \simeq \frac{1.47 \times 10^8\; E^{3/2}\,({\rm keV})}{n\,({\rm cm}^{-3})}.$$

Even for the highest initial energy ~300 keV and a density in the lower corona ~10^{11} cm^{-3} this formula gives a decay

time about ~7 s. However, most electrons have energies much smaller than 300 keV, and those that are not trapped in the corona deposit their energy in the much denser plasma in the chromosphere. Then a real decay time for the precipitating electrons that are considered in this paper is about ≤1 s. Therefore, if the characteristic time of the beam variations is more than a few seconds, one can consider the beam electron dynamics as a sequence of quasi-steady states of beams injected every second with different initial beam parameters at the injection point. This is the approach taken for the kinetic problem solution in the present paper.

2.5. Normalization of the distribution function

In order to define a scaling parameter K in the normalization (1) of a distribution function f one has to calculate the initial energy flux $F(\xi_{\min})$ carried through the top boundary by beam electrons with a given spectral index γ, and lower and upper energy cut-offs $E_{\rm low}$ and $E_{\rm upp}$. The particle density at the top boundary can be defined as follows:

$$N(\xi_{\min}) = F(\xi_{\min}) \frac{\int_{E_{\rm low}}^{E_{\rm upp}} \int_{-1}^{1} E^{-\gamma-0.5} \exp\left(-\left(\frac{\mu-1}{\Delta\mu}\right)^2\right) {\rm d}E{\rm d}\mu}{\sqrt{\frac{2}{m_{\rm e}}} \int_{E_{\rm low}}^{E_{\rm upp}} \int_{-1}^{1} E^{-\gamma+1} \exp\left(-\left(\frac{\mu-1}{\Delta\mu}\right)^2\right) \mu {\rm d}E{\rm d}\mu}, \quad (14)$$

where the beam energy flux at the top boundary is expressed as:

$$F(\xi_{\min}) = K \sqrt{\frac{2}{m_{\rm e}}} \int_{E_{\rm low}}^{E_{\rm upp}} \int_{-1}^{1} E^{-\gamma+1} \exp\left(-\left(\frac{\mu-1}{\Delta\mu}\right)^2\right) \mu {\rm d}E{\rm d}\mu,$$

and the scaling factor K is dependent on beam parameters as given by the formula:

$$K = \frac{F(\xi_{\min})}{\sqrt{\frac{2}{m_{\rm e}}} \int_{E_{\rm low}}^{E_{\rm upp}} \int_{-1}^{1} E^{-\gamma+1} \exp\left(-\left(\frac{\mu-1}{\Delta\mu}\right)^2\right) \mu {\rm d}E{\rm d}\mu}. \quad (15)$$

2.6. The hard X-ray emission

The resulting hard X-ray bremsstrahlung or HXR photon flux produced in the magnetic field direction is defined by the following expression:

$$I(\varepsilon) = 2\pi A_x K \int_{\xi_{\min}}^{\xi_{\max}} \int_{\varepsilon}^{\infty} \int_{-1}^{1} f(\xi, \eta, \mu)\, \eta\, \sigma^{\rm B}(\eta, \varepsilon)\, {\rm d}\mu {\rm d}\eta {\rm d}\xi \quad (16)$$

where X is the ionisation degree and $\sigma^{\rm B}$ is the bremsstrahlung differential cross-section as follows:

$$\sigma^{\rm B}(\eta, \varepsilon, \mu) = \frac{{\rm d}^2\sigma_{\parallel}}{{\rm d}\Omega {\rm d}(h\nu)} + \frac{{\rm d}^2\sigma_{\perp}}{{\rm d}\Omega {\rm d}(h\nu)}.$$

The constant A_x is defined as follows

$$A_x = \frac{S}{4\pi R^2} \frac{2E_0}{m_{\rm e}},$$

Table 1. Beam particle densities for beams with power-law energy spectra for different sets of initial energy flux and spectral indices.

Flux, erg cm^{-2} s^{-1}	10^8	10^{10}	10^{12}
γ	Particle density, cm^{-3}		
3	2.2×10^5	2.2×10^7	2.2×10^9
5	3.4×10^5	3.4×10^7	3.4×10^9
7	4.8×10^5	4.8×10^7	4.8×10^9

where S is the flare area, and R is the distance to the observer.

The differential cross-sections of electron scattering in the directions parallel and perpendicular to the magnetic field, $\sigma_{\parallel}^{B}$ and $\sigma_{\perp}^{B}$, were calculated as follows (Elwert & Haug 1970; Nocera et al. 1985):

$$\frac{{\rm d}^2\sigma_{\parallel}}{{\rm d}\Omega {\rm d}(h\nu)} = C\left(A + B\left(1-\mu^2\right)\right)\sigma_0,$$
$$\frac{{\rm d}^2\sigma_{\perp}}{{\rm d}\Omega {\rm d}(h\nu)} = CA\sigma_0,$$

where the parameters A, B, C are defined as follows:

$$A = \frac{\eta - \varepsilon/2}{\eta(\eta-\varepsilon)} \ln \frac{\sqrt{\eta} + \sqrt{\eta-\varepsilon}}{\sqrt{\eta} - \sqrt{\eta-\varepsilon}} - 1,$$
$$B = \frac{\frac{3}{2}\varepsilon - \eta}{\eta(\eta-\varepsilon)} \ln \frac{\sqrt{\eta} + \sqrt{\eta-\varepsilon}}{\sqrt{\eta} - \sqrt{\eta-\varepsilon}} + 3,$$
$$C = \frac{1}{\eta\varepsilon} \frac{1 - \exp\left(-\frac{2\pi\alpha c\sqrt{m_{\rm e}}}{\sqrt{2\eta E_{\rm low}}}\right)}{1 - \exp\left(-\frac{2\pi\alpha c\sqrt{m_{\rm e}}}{\sqrt{2(\eta-\varepsilon)E_{\rm low}}}\right)},$$

where ε is a dimensionless photon energy $h\nu/E_{\rm low}$, and the elementary cross-section σ_0 is defined as follows:

$$\sigma_0 = \frac{1}{137} \frac{1}{2\pi} \frac{mc^2}{E_{\rm low}^2} r_0^2,$$

where r_0 is the classical electron radius.

2.7. The adopted parameters

The calculations were done for beam electrons with power-law energy spectra with a lower energy cut-off $E_{\rm low}$ = 16 keV and upper energy cut-off $E_{\rm upp}$ = 384 keV, or $\eta_{\max}$ = 24, which was taken arbitrarily large to investigate electron precipitation into deeper atmospheric levels. In this paper we ignore the relativistic effects for the precipitation of these higher energy electrons, since we concentrate on the interpretation of the lower energy photon spectra affected by Ohmic losses. Spectral indices were adopted equal to 3, 5 or 7, the initial energy fluxes were adopted as 10^8, 10^{10} or 10^{12} erg cm^{-2} s^{-1}. Two types of pitch-angle distribution were considered: a "thin distribution" ($\Delta\mu$ = 0.1) and "wide distribution" ($\Delta\mu$ = 0.6).

In Table 1 the corresponding beam initial densities at the top boundaries are presented calculated according to Eq. (14) in Sect. 2.5.

3. Results and discussion

3.1. The beam electron distribution functions

3.1.1. The effect of energy diffusion

In order to investigate the energy diffusion effect for pure collisions of beam electrons with charged particles (ions and electrons) and neutrals, let us consider a solution of Eq. (10) where all terms are neglected except for the second term on the left-hand side and second term on the right-hand side. Then the equation becomes a continuity equation, which has been solved analytically by Syrovatskii & Shmeleva (1972).

The total density variations with depth (in cm^{-3}) are plotted for mono-energetic beams injected along a magnetic field direction in Fig. 1a, and the differential density variations with depth are plotted in Fig. 1c for a beam injected with a power-law initial energy distribution with spectral index $\gamma = 3$.

Apparently, the energy of mono-energetic electron beams decreases gradually with column density growth because of energy diffusion as follows (Syrovatsky 1968; Syrovatsky & Shmeleva 1972):

$$E^*(\xi) = \sqrt{E^2 - 2a\xi}, \tag{17}$$

where a is the collisional parameter described and estimated in Sect. 2.3.

As a result, the density of a mono-energetic beam decreases parabolically with depth according to the formula above, as shown in Fig. 1a. Obviously, electrons with an initial energy of $E_{\rm low} = 16$ keV precipitating into a fully ionised plasma lose their energy completely at a depth of $\xi = 4.7 \times 10^{19}$ cm^{-2} while for those with energy $E_{\rm upp} = 380$ keV the energy will only be reduced to $E^*_{\rm upp}(\xi) = 372$ keV. Electrons with an energy of 380 keV lose their energy completely at a column density of $(2.8\text{–}3.3) \times 10^{22}$ cm^{-2} where the first value corresponds to a fully ionised plasma and the second to a partially ionised one with an ionisation degree $X = 0.001$. This means that the lower energy electrons are becoming fully thermalized to the ambient plasma energies below column density $\xi = 4.7 \times 10^{19}$ cm^{-2} while the electrons with higher energy can reach the photospheric depth of 3.3×10^{22} cm^{-2}. Obviously, if the energy diffusion is neglected, then the energy delivered by beam electrons to a given depth can be strongly overestimated (Mauas & Gomez 1997).

The energy diffusion effect on a power-law electron beam injected from the top can be investigated from Eq. (2), or (9) in the dimensionless form by neglecting all the terms except one on the left hand side containing $\frac{\partial}{\partial s}$ and one on the right hand side containing $\frac{\partial}{\partial \eta}$. Then Eq. (9) becomes similar to the continuity equation solved analytically by Syrovatskii & Shmeleva (1972) for a fully ionised plasma and extended by Zharkova & Kobylinskii (1993) for a partially ionised plasma. It is solved numerically for electron beam precipitation into a fully ionised plasma using the method of finite elements with a combination of explicit and implicit schemes as described in the paper by Gordovsky & Zharkova (2003). The beam differential spectra, i.e. differential densities calculated as an integral over pitch angles of the electron distribution functions at given depths are presented in Fig. 1c.

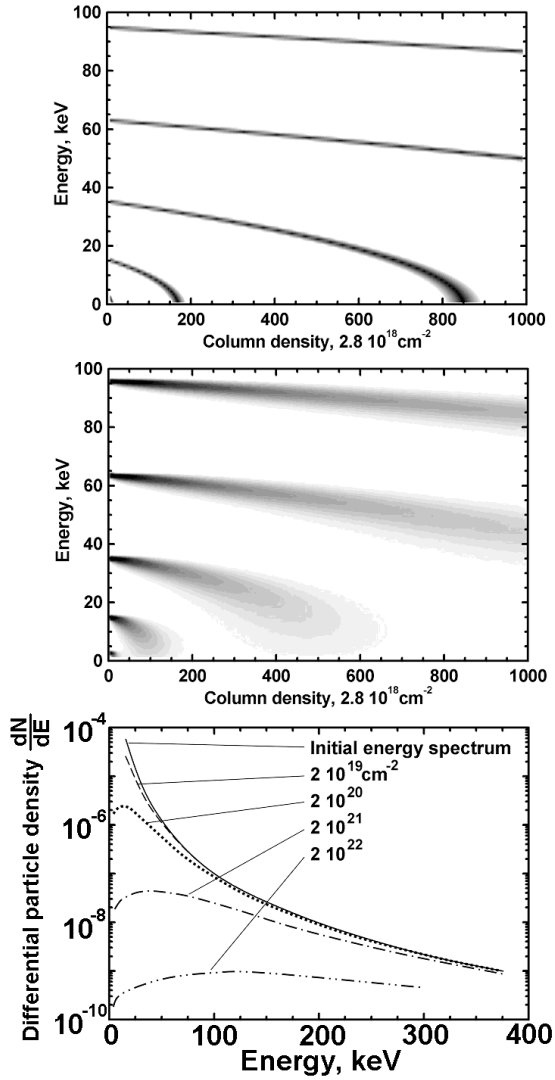

Fig. 1. The energy and pitch-angle diffusion: **a)** – depth variations of the initially mono-energetic beams with energies 4, 16, 36, 64 and 96 keV losing energy in pure Coulomb collisions without pitch-angle diffusion; **b)** – the same as in **a)** but with pitch-angle diffusion; **c)** – depth variation of a beam injected with a power-law spectrum ($E_{\rm low}$ = 16 keV, $E_{\rm upp}$ = 384 keV and γ = 3). The beam differential spectra ($\frac{\mathrm{d}N}{\mathrm{d}E}(\xi, E)$) versus energy plotted for different column densities from the corona (dashed and dotted lines), to transition region (dash-dotted line) and chromosphere (dash-dot-dotted and short-dashed lines).

It can be seen that the energy diffusion is stronger for lower-energy electrons, since, as follows from Eq. (10), the following proportion is valid $\mathrm{d}\eta/\mathrm{d}s \propto \eta^{-1}$. With every depth step this leads to a growing deficit of low-energy electrons in comparison with the initial energy spectrum, that, in turn, appears in the electron differential spectra as a "flattening" at lower energies. In Fig. 1c there are a few examples demonstrating that at larger column depths the initial power-law energy distribution with a spectral index $\gamma = 3$ is transformed into the distributions with a flat lower energy part, which becomes even flatter with every step in depth. This flattening in the electron

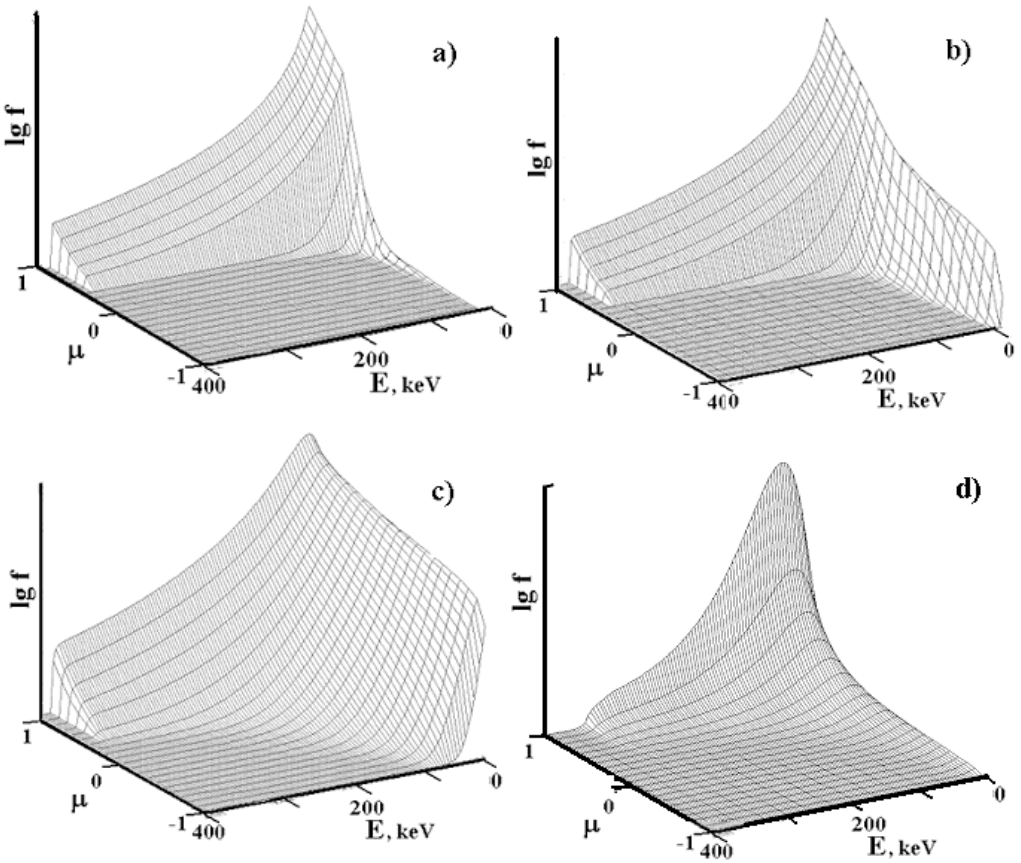

Fig. 2. Energy – pitch-angle ($E-\mu$) distributions (the vertical axis) versus energy E and pitch-angle cosines μ calculated without a return current effect for beams injected with the energy range 16–384 keV, spectral index $\gamma = 3$ and initial energy flux 10^{10} erg cm^{-2} s^{-1}. **a)** Corresponds to column density 1.8×10^{18}; **b)** to 1.3×10^{19}; **c)** to 5.1×10^{20}; and **d)** to 2.9×10^{22} cm^{-2}.

differential spectra can result in the flattening of the integrated (over depth) electron spectrum, i.e. of the total number of electrons with a given energy at a given instance. If there are any additional electron energy sinks, such as pitch-angle diffusion or Ohmic heating, they can speed up further the electron diffusion in energy and result in a noticeable spectrum flattening (see Sects. 3.1.2 and 3.1.3). This kinetic property of the beam precipitation can strongly affect the hard X-ray bremsstrahlung emitted from a whole flaring atmosphere that will be discussed in Sect. 3.3.

3.1.2. The effect of pitch-angle diffusion

Now, in order to investigate the effect of pitch-angle diffusion on the electron distribution functions for pure Coulomb collisions, let us consider Eq. (10) where all the terms are neglected except for the second term on the left-hand side and the second, third and fourth terms on the right-hand side, i.e. taking into account both the energy diffusion (Fig. 1a) and anisotropic scattering, or pitch-diffusion (Fig. 1b).

It can be seen that the mono-energetic beams precipitating with pitch-angle diffusion reveal, first, that the decrease of energy with depth caused by diffusion is much steeper than parabolic (Fig. 1a), and, second, that it sets in at much smaller depths (Fig. 1b). Apparently, this happens because the beam electrons, which lose their energy in Coulomb scattering, can be scattered many times not only forward ($\mu > 0$) but backwards ($\mu < 0$). This results in the electrons losing much more energy during their propagation, so that they will have lost all their energy at much lower column densities depending on the pitch-angles gained during their precipitation. The pitch-angle diffusion is effective for electrons at any energy, while it is stronger for low energy electrons (the lower curves) than for the higher energy ones (compare grey areas in upper and lower curves in Fig. 1b).

For a beam injected with a power-law energy spectrum that loses its energy in pure Coulomb collisions the distribution functions with pitch-angle diffusion in the $E-\mu$ coordinates is shown in Fig. 2 for an initial flux 10^{12} erg cm^{-2} s^{-1}, $\gamma = 3$, lowest and highest energies 16 and 386 keV, respectively. Because of pitch-angle diffusion the number of lower energy electrons increases with depth and changes from a narrow angular distribution at the injection point to a much wider one in deeper layers becoming nearly isotropic at larger atmospheric depths below $\xi = 2 \times 10^{22}$ cm^{-2}.

3.1.3. The effect of an induced electric field

The effect of Ohmic energy losses and pitch-angle diffusion can be considered taking into account all but the first terms on the left hand side and all but the first and last terms on the right-hand side of Eq. (10). This takes into account energy and

pitch-angle diffusion owing to collisions and Ohmic heating without magnetic field convergence.

The effect of the return current on the electron distribution functions is demonstrated in Figs. 3–6 for electron beams with the accepted parameters (see Sect. 2.7).

Similar to Zharkova et al. (1995), the effect of the electric field induced by a precipitating beam is essential for the initial beams with a wide pitch-angle dispersion at injection, $\Delta\mu = 0.6$ (see the initial condition in Sect. 2.4).

The return current effect appears at very high depths in the corona or the transition region as an additional maximum at negative pitch-angles in the electron distributions with lower energies (E < 50–90 keV). For moderate beams with an initial energy flux of 10^{10} erg cm^{-2} s^{-1} the return current appears at a depth of $\xi = 1.8 \times 10^{18}$ cm^{-2} for a harder beam (Fig. 3) or even higher at $\xi = 1.2 \times 10^{18}$ cm^{-2} for a softer beam (Fig. 4). The return current is maintained during the beam precipitation downwards into the transition region, $\xi = 4.0 \times 10^{19}$ cm^{-2} (Fig. 4), or even into the upper chromosphere $\xi = 1.0 \times 10^{20}$ cm^{-2} (Fig. 3) and then disappears at the lower chromosphere because of a decrease of the ambient plasma conductivity caused by a drop in the degree of plasma ionisation. For harder beams the returning electrons become fully isotopic in pitch-angle at the upper chromospheric depth, $\xi = 1.0 \times 10^{20}$ cm^{-2} for moderate initial fluxes (Fig. 3) and even just below the transition region at $\xi = 4.0 \times 10^{19}$ cm^{-2} for higher initial energy fluxes of 10^{12} erg cm^{-2} s^{-1} (Fig. 5). For more intense beams with an initial energy flux of 10^{12} erg cm^{-2} s^{-1} the return current appears immediately after the beam injection at a depth of $\xi = 1.2 \times 10^{18}$ cm^{-2} for a harder beam (Fig. 5) or $\xi = 1.0 \times 10^{18}$ cm^{-2} for softer beam (Fig. 6), it is maintained during the beam precipitation downwards to the transition region, $\xi = 2.0 \times 10^{19}$ cm^{-2} (Fig. 6), or into the upper chromosphere $\xi = 9.0 \times 10^{19}$ cm^{-2} (Fig. 5).

The density of the returning beam is less than that of the precipitating one of moderate intensity by two orders of magnitude for harder, and by a factor 2–3 for softer beams (compare Figs. 3 and 4) while for intense beams the density of the returning beam becomes comparable with that of the direct one (Figs. 3 and 5 or 4 and 6). This result is different from the previous calculations by Zharkova et al. (1995) where the intense beams were found to completely return to the source in the corona. We estimate that this difference is related to the inclusion in the current paper of the ambient plasma electrons into the return current calculations in the system of kinetic (2) and Ampere Eqs. (6) (see Sect. 2.2) which is in our view a more reasonable approach. It appears that the ambient electrons play an essential role in compensating the electric field induced by precipitating electrons, especially at higher depths where there are not enough back-scattered electrons produced by pitch-angle diffusion (see Sect. 3.1.2). As a result, at higher depths the return current is mostly formed by the ambient plasma electrons, which is clearly seen in the top panels in Figs. 3–6.

The energy distributions of the return current "bump" are limited to energies lower than ~45–50 keV for softer beams ($\gamma \approx 7$) (Figs. 4, 6) then increases to 65–70 keV for harder beams ($\gamma \approx 3$) (Figs. 3, 5). The energy distributions of returning electrons appear to be exponential with a maximum of 15 keV for a weaker soft beam, which shifts to higher energies, 20–25 keV, for harder and more intense beams. This is likely to be caused by a combination of much more effective pitch-angle and energy diffusion for lower energy than for higher energy electrons (see Sects. 3.1.1 and 3.1.2), which leads to a maximum in the returning electron number dependent on the formation depth of the return current. These returning electrons can significantly contribute to the resulting photon spectra that will be discussed in Sect. 3.3.

Comparing the precipitating electron distribution functions in Figs. 3–6 after the return current effect ceases, it is seen that at higher column densities in the lower chromosphere lower energy electrons (≤100 keV) become fully isotropic. This result confirms the conclusions about beam thermalisation by Leach & Petrosian (1981) and Zharkova et al. (1995). However, the depth of thermalisation found by Leach & Petrosian is ~3×10^{21} cm^{-2}, while in Zharkova et al. (1995) and the present simulations the results show that the thermalisation occurs deeper, at a depth of about ~10^{22} cm^{-2} even after taking into account the effect of Ohmic energy losses. This discrepancy can be explained either by the different forms of collisional energy losses proposed in these papers or more likely, by the absence of energy diffusion in the boundary conditions for the numeric solutions of the kinetic equation used by Leach & Petrosian (1981), which leads to a faster energy smoothing with depth.

3.2. Particle and energy flux

Using the electron distribution functions above one can calculate the depth variations of density and energy fluxes for precipuitating electron beams according to formulae (12) with the normalisation coefficient K determined through the initial beam parameters (Eq. (13)).

3.2.1. The effect of non-uniform target ionisation

The energy diffusion in the partially ionised plasma is defined by a parameter a (Eq. (9)). Normally, this parameter as well as all the Coulomb logarithms for electrons, ions and neutral atoms are taken to be constant at all depths. However, for the partially ionized ambient plasma, i.e. in the lower chromosphere and photosphere, this is not strictly valid. In the lower chromosphere the ionisation degree of the ambient plasma strongly decreases to 10^{-3}–10^{-4} (Zharkova & Kobylinskii 1993), which is demonstrated in Fig. 7a, and leads to a sharp decrease in the number of electrons and ions in the lower chromosphere. Keeping in mind that the electron energy changes with depth following Eq. (17), the smaller the parameter a the lower the particle energy loss. It leads to a slower beam dissipation at larger depths and to an increase in the maximum penetration depth for electrons with the same energy as those precipitating into a fully-ionised ambient plasma.

This leads to an increase of the collision frequency with neutral atoms and a decrease of the collisional parameter a defining the fraction of energy that each electron loses at a given depth (see estimations in Sect. 2.3). This is clearly seen in Fig. 7b, which demostrates the depth variations of the

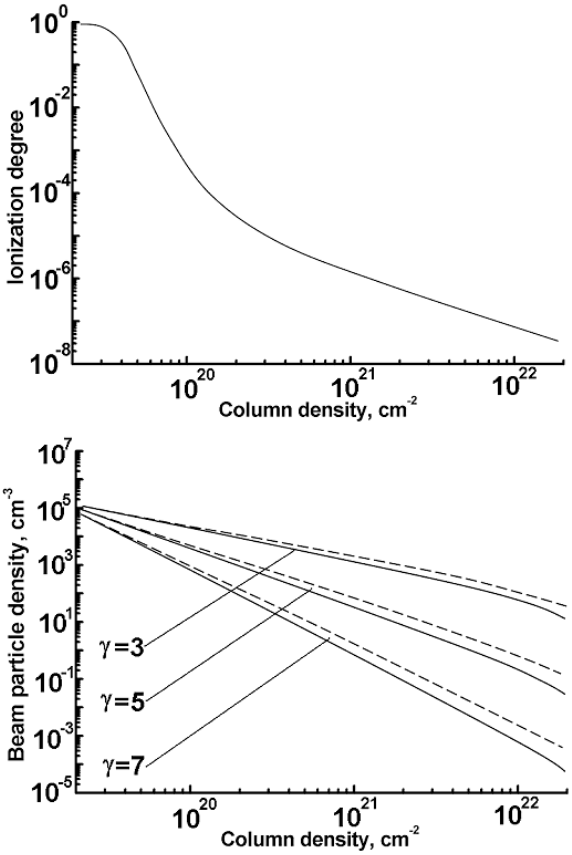

Fig. 7. The variations of **a)** the ionisation degree with depth from Zharkova & Kobylinskii 1993 and **b)** the beam density with depth for initial beam flux $F_0 = 10^8$ erg cm^{-2} s^{-1} for different initial spectral indices. The solid curves correspond to beam densities in a fully ionized atmosphere, the dashed curves correspond to beam densities in the plasma with ionization degree profile as in **a)**.

electron beam density corresponding to a fully ionized target (solid lines) and to a target with partial ionisation (dashed lines). In a partially ionised plasma the density of beam electrons precipitating to a given depth is higher than in a fully ionized plasma. This is apparently caused by less efficient electron scattering on neutral atoms, which allows more electrons to reach deeper atmospheric layers in the chromosphere and photosphere.

3.2.2. The effect of Ohmic energy losses

Figures 8 and 9 give the beam particle densities and energy fluxes computed for electron beam precipitation into the partially ionized ambient plasma taking into account energy and pitch-angle diffusion for collisional and Ohmic energy losses in a magnetic field with a fixed convergence of 10. The left upper panel presents the case without electric field while the right upper and two lower panels are produced for beams with spectral indices 3, 5 and 7 and initial energy fluxes of 10^8, 10^{10} and 10^{12} erg cm^{-2} s^{-1}, respectively.

Since the beam density and energy flux at a given depth are an integral of the distribution function with a normalisation coefficient K including a factor of the initial energy flux F_0 (discussed in Sect. 3.1.3), an increase of the beam initial energy flux is expected to lead to a proportional increase of its density and energy flux, which is clearly seen from a comparison of the panels a–d in Figs. 8 and 9 for different initial fluxes. By comparing the upper right and lower left panels one can see that without Ohmic losses the beam densities at every depth are much higher than with them. Also without electric field losses the beams reach much deeper layers, below 10^{22} cm^{-2}, in comparison with the depth of 10^{21} cm^{-2} for $\gamma = 3$ when the electric field is taken into account.

With further precipitation to deeper layers, softer beams with higher spectral indices (solid curves) have much lower densities and they reach much lower depths than harder beams with a lower index $\gamma = 3$ (dot-dashed curves). With the inclusion of the electric field the densities become even lower for beams with $\gamma = 7$, which reach smaller depths of 10^{21} cm^{-2} (right upper panel) instead of 2×10^{22} cm^{-2} without electric field (right lower panel). This reflects higher energy losses in the denser atmosphere layers owing to energy diffusion by a softer beam, which thermalises much faster than a hard one (see Sect. 3.1.1); this effect becomes even stronger if the electric field is taken into account (see Sect. 3.1.3).

In summary, the most important effect revealed in Fig. 8 is the dependence of beam density variations with depth on the beam's initial spectral index that can be followed for the different curves in every panel. At any depth in the corona with or without electric field the beam densities are lower for a spectral index of 3 than for one of 7. This reflects the effect of pitch-angle diffusion, which is more pronounced for harder beams in lower density plasmas and becomes even higher when Ohmic losses are taken into account (compare plots c) and d)). This happens because of the electric field effect, which is closely related to the pitch-angle scattering of direct electrons and to the proportion of thermal and precipitating electrons in the return current beam. Since the electric field induced by harder beams is higher than that induced by softer ones (see Sect. 3.1.3), for harder beams there are more beam electrons returning to the source and fewer precipitating electrons moving downwards to the chromosphere.

The density variations discussed above are clearly reflected in depth variations of beam energy fluxes presented in Fig. 9. The energy flux without electric field (panel d)) shows a smooth decrease with depth, which is steeper for the softer beam with $\gamma = 7$ and flattens when the index decreases to 3. The inclusion of the electric field for beams with the same initial energy flux of 10^{10} erg cm^{-2} s^{-1} reveals that the beam energy flux with spectral index 7 decreases much faster at the transition region and upper chromosphere where Ohmic losses have a maximum (see Sect. 3.1.3), and becomes flatter in deeper layers. The softer beams with higher indices show a flux, that decreases more steeply with electric field (Fig. 9c) than do those without it (Fig. 9d).

3.2.3. The effect of a converging magnetic field

Electron precipitation in a converging magnetic field is expected to lead to a deflection and magnetic mirroring of electrons of the precipitating beam. In a first approach the effect of

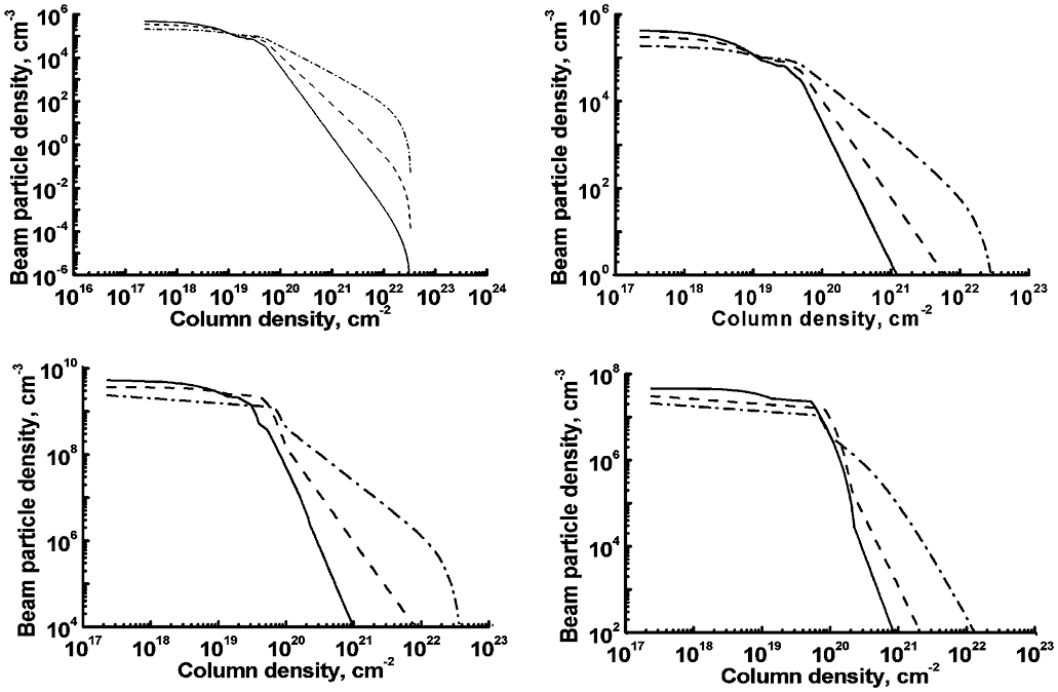

Fig. 8. The beam particle density variations with depth calculated without electric field **a)** for an initial energy flux of 10^{10} erg cm^{-2} s^{-1} and with an induced electric field, for the initial energy fluxes 10^{8} erg cm^{-2} s^{-1} **b)**, 10^{10} erg cm^{-2} s^{-1} **c)** and 10^{12} erg cm^{-2} s^{-1} **d)** and for initial spectral indices 7 (solid curves), 5 (dashed curves) and 3 (dot-dashed curves).

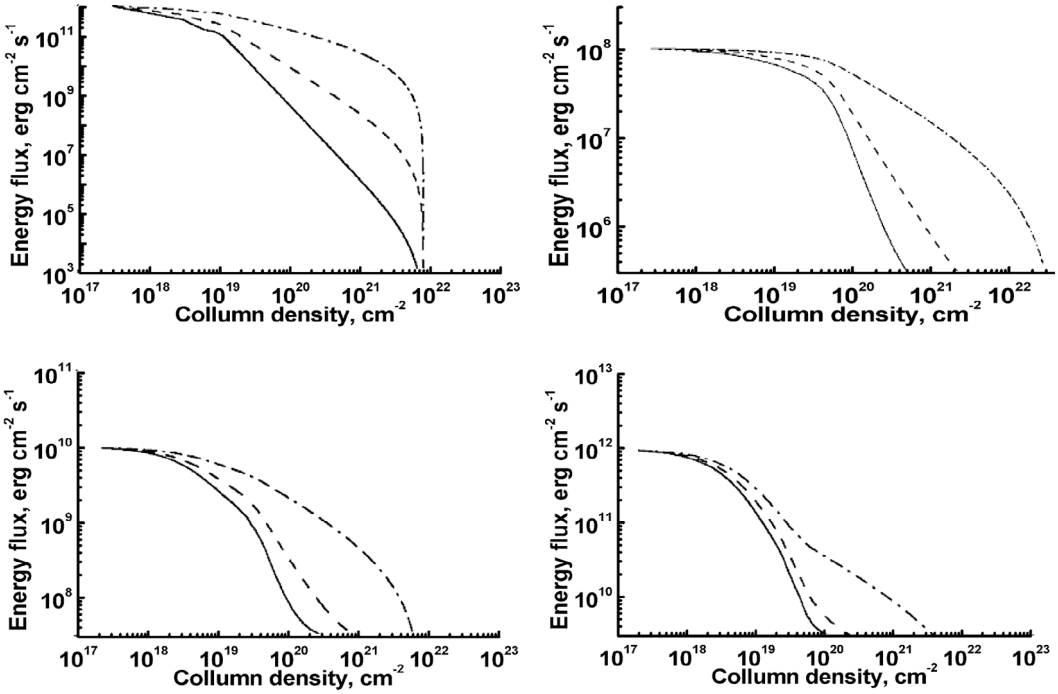

Fig. 9. The beam energy flux variations. The plots **a)**–**d)** correspond to the same models as in Fig. 8.

magnetic field convergence can be estimated in the "pure magnetic field" approach similarly to Leach & Petrosian (1981). Neglecting all the terms in Eq. (9) except for the second one on the left-hand side and the last term on the right-hand side, one can obtain:

$$\mu\eta^2\frac{\partial f}{\partial s} = \frac{\eta^2\left(1-\mu^2\right)}{2}\frac{\partial \ln B}{\partial s}\frac{\partial f}{\partial \mu}. \tag{18}$$

This can be solved analytically by a separation of variables as follows:

$$f(\xi,\mu) = f_0 \exp\left[\lambda \ln\frac{B(\xi)}{B(0)}\right]\left(1-\mu^2\right)^{-2\lambda}, \tag{19}$$

where f_0 is a normalization constant. The parameter λ defines the width of the initial distribution over pitch-angle and is

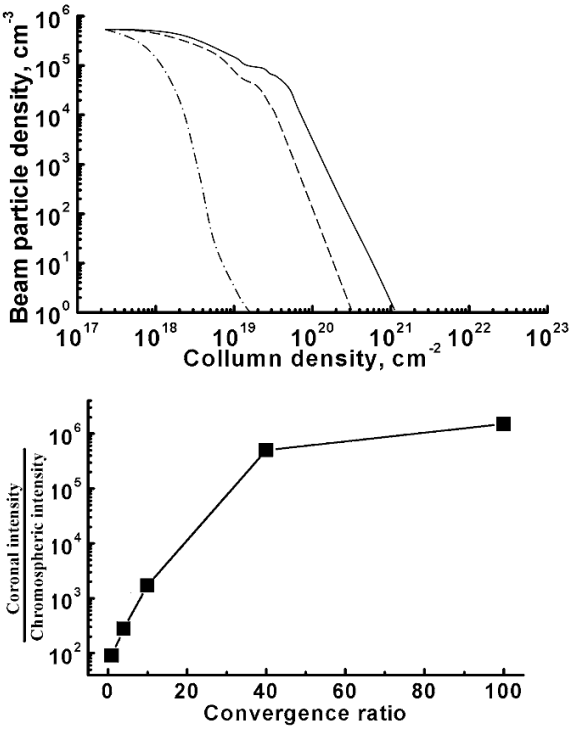

Fig. 10. The effect of the converging magnetic field. **a)** – The beam particle density variations versus column density for initial spectral index $\gamma = 3$ and initial energy flux $F_0 = 10^8$ erg cm^{-2} s^{-1} precipitating in a magnetic field converging with a factor of 10 (dot-dashed line) and with a factor of 100 (dotted line). The beam particle densities for a beam precipitating in a non-converging field is plotted by a solid line. **b)** – The ratio of the total non-thermal bremsstrahlung intensity produced in the corona (2×10^{17} cm^{-2}–2×10^{20} cm^{-2}) to that in the chromosphere (>2×10^{20} cm^{-2}) versus magnetic field convergence rate α.

related to the half-width as follows: $\lambda = 1$ corresponds to $\Delta\mu \approx 0.1$, $\lambda = 0.5$ to $\Delta\mu \approx 0.2$ and $\lambda = 0.1$ corresponds to $\Delta\mu \approx 0.4$.

The total particle density (integrated over pitch-angle in Eq. (19)) can be expressed through the initial particle density $N(\xi = 0)$ as follows:

$$N(\xi) = N(\xi = \xi_{\min}) \left(\frac{B(\xi)}{B(\xi = \xi_{\min})} \right)^{\lambda}. \quad (20)$$

The depth variations of electron beam densities are plotted in Fig. 10, calculated for an electron beam injected with $\gamma = 3$, $F_0 = 10^8$ erg cm^{-2} s^{-1} and initial pitch-angle cosine dispersion 0.2 ("narrow" beam), which precipitates with Coulomb and Ohmic energy losses into a converging magnetic field. It should be noted that precipitation of a beam into a magnetic field converging with a factor $\alpha = 10$ does not affect the distribution functions significantly (not presented here; see Leach & Petrosian 1981). However, the integrated effect of magnetic convergence on the beam particle density (Fig. 10) reveals that the latter decreases much faster with depth for a magnetic field with higher convergence rate ($\alpha = 10$ or 100), confirming that there is substantial magnetic trapping in the upper layers of the corona, similar to the results by Leach & Petrosian (1981) and McClements (1992a). However, at the lower chromospheric levels in a weakly ionised plasma, where the main channels of energy loss are collisions with neutrals, a converging magnetic field helps to collimate the precipitating beams and allows electron beams to penetrate to deeper chromospheric levels, even to the photosphere.

Table 2. The comparison of the spectral indices in "broken" HXR spectra. The low-energy indices $\delta_{\rm low}$ are measured between 10 and 40 keV, while high-energy indices $\delta_{\rm high}$ are measured in the range 80–240 keV.

Flux, erg cm^{-2} s^{-1}	10^8		10^{10}		10^{12}	
γ	$\delta_{\rm low}$ / $\delta_{\rm high}$					
3	4.3	4.4	3.1	4.4	1.8	4.4
5	6.1	6.4	4.1	6.4	2.9	6.3
7	7.8	8.3	5.3	8.3	3.9	8.2

3.3. The hard X-ray photon spectra

3.3.1. The return current effect

The HXR bremsstrahlung, or photon spectra, emerging from a flaring atmosphere, are calculated in the direction parallel to the magnetic field using the electron distribution functions above with respect to Eq. (16). The examples of photon spectra are presented in Fig. 11 for beams with the initial energy fluxes of 10^8 erg cm^{-2} s^{-1} (a), 10^{10} erg cm^{-2} s^{-1} (b) and 10^{12} erg cm^{-2} s^{-1} (c) and spectral indices $\gamma = 3$, 5, 7 for the models with and without inclusion of the return current effect. The photon spectral index is found to be higher than those of electron beams by 1.5 for weak and moderate beams and by 1.2–1.3 for softer and very intense ones. The photon indices are different from those (of ~0.5) reported by Syrovatsky & Shmeleva (1972), which is likely to be due to the addition of pitch-angle diffusion and Ohmic losses.

However, if the return current is taken into account, the hard X-ray spectra reveal flattening at lower energies (10–40 keV), while remaining close to the initial beam spectral index in the middle energy range (70–200 keV). Since the changes of the electron distributions in the higher energy tail are related to a non-relativistic factor, which we do not consider in the current paper, here we concentrate on the index changes at lower energies. In Table 2 the photon spectral indices for lower ($\delta_{\rm low}$) and higher ($\delta_{\rm high}$) energy ranges deduced from the initial precipitating beam indices γ (first column) and energy fluxes (first row) are presented in Table 2.

By analysing Fig. 11 and the spectral indices from Table 2 one can conclude that the resulting hard X-ray photon spectra calculated with the return current effect are broken power-law (elbow-type) spectra as very often observed. The higher energy part (≥50 keV) retains the spectral index $\delta_{\rm high}$ that it had without the electric field (see the first paragraph of this section), i.e. it is increased with respect to the beam spectral index γ by 1.5 for weaker and harder beams (10^8–10^{10} erg cm^{-2} s^{-1}, $\gamma \simeq$ 3–5) or by 1.2–1.3 for more intense and softer beams (10^{11}–10^{12} erg cm^{-2} s^{-1}, $\gamma \simeq$ 5–7). The flattening of the spectral index at lower energies increases with increasing initial beam energy flux (compare

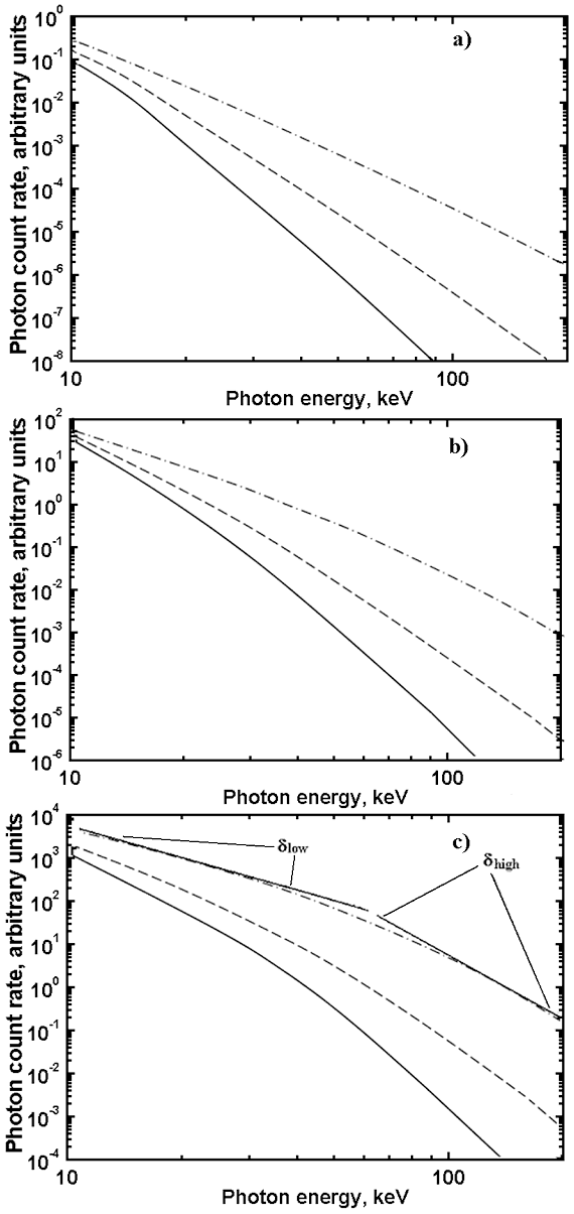

Fig. 11. The HXR bremsstrahlung spectra produced by precipitating electrons with different sets of initial energy flux and spectral indices. In panel **a)** we show spectra for initial flux 10^8 erg cm^{-2} s^{-1}, **b)** 10^{10} erg cm^{-2} s^{-1} and **c)** 10^{12} erg cm^{-2} s^{-1}. The solid lines correspond to the initial beam spectral index $\gamma = 7$, dashed to $\gamma = 5$ and dot-dashed to $\gamma = 3$. The photon spectral indices measured using these spectra are presented in Table 2.

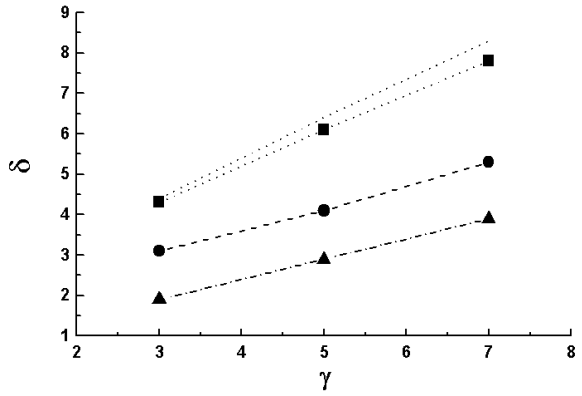

Fig. 12. Variations of the bremsstrahlung photon spectral indices δ for beams with different initial energy flux (see Table 2). The indices $\delta_{\rm high}$ of the higher energy part of the spectra (which is not dependent on the energy flux) are shown by the dotted line. The indices $\delta_{\rm low}$ of the lower energy part of the spectra are shown for initial energy fluxes 10^8 erg cm^{-2} s^{-1} (the solid lines with squares), 10^{10} erg cm^{-2} s^{-1} (the dashed line with circles) and 10^{12} erg cm^{-2} s^{-1} (the dash-dotted line with triangles).

plots a) and c) in Fig. 11) and with decreasing spectral index (compare the solid and dot-dashed curves in each panel).

The most important result is that the lower energy part of the X-ray photon spectra reveals a very small increase or even a substantial decrease of its spectral index $\delta_{\rm low}$ with respect to the beam spectral index γ (see Fig. 12 and Table 2, Cols. 2, 4, 6). For instance, for a weaker beam (10^8 erg cm^{-2} s^{-1}) $\delta_{\rm low}$ is higher than γ by 1.3 for $\gamma = 3$, by 1.1 for $\gamma = 5$ and 0.8 for γ=7. For moderate beams (10^{10} erg cm^{-2} s^{-1}) with $\gamma = 3$ the photon index δ is still increased but only by 0.1 for $\gamma = 3$ while for softer beams with $\gamma = 5$, δ is equal to 4.1 and for $\gamma = 7$ it is reduced to 5.3. For the intense beam (10^{12} erg cm^{-2} s^{-1}) the photon index $\delta_{\rm low}$ becomes equal to 1.8, 2.9 and 3.9 for beam indices γ of 3, 5 and 7, respectively. This means that with an increase in the initial energy flux to $\sim 10^{12}$ erg cm^{-2} s^{-1} of the electron beam producing the photon spectra the difference between the beam index and the lower energy photon spectral index becomes negative, i.e., the photon index is lower by 1.2 for harder beams and by 3.1 for softer beams. This is a result of the increased strength of the induced electric field that enhances the energy and pitch-angle diffusion for softer intense electron beams, as was discussed in Sect. 3.1.3.

The initial energy flux of the precipitating beam also defines the energy in the HXR photon spectra where its spectral index changes: the "break" energy. For instance, if the initial flux is about 10^{10} erg cm^{-2} s^{-1} then this energy is about 40–50 keV, while if the initial flux increases to 10^{12} erg cm^{-2} s^{-1}, the break energy moves to 50–70 keV. This dependence of the break energy on the initial flux can be explained by an increase of a number of higher energy electrons in the return current with a growth in the initial electron beam flux, as was discussed in Sect. 3.1.3.

3.3.2. The effect of magnetic field convergence

Based on the analysis of particle densities at given depth for beams precipitating into a converging magnetic field discussed in Sect. 3.2.3 let us calculate the coronal and chromospheric HXR emission produced by beam electrons, by separating them at the bottom of the transition level at a depth of $\xi = 5 \times 10^{19}$ cm^{-2}. Then we integrate this emission over depth and energy, produce the coronal-to-chromospheric ratio and plot it versus the magnetic field convergence parameter α as shown in Fig. 10. Following a substantial beam density decrease with the increase of magnetic field convergence from 1 to 100, the resulting ratio of the integrated photon emission produced in

the corona to that in the chromosphere sharply increases with increasing convergence until the convergence reaches 40, after which the increase is less noticeable and even tends to saturate.

The increase of this ratio with magnetic field convergence confirms that magnetic trapping plays a significant role in the formation of HXR spectra from solar flares, which, if not taken into account, can lead to the overestimation of the power of beam electrons producing this emission. This effect can also account for more frequent occurrence of coronal HXR emission in the upper levels of a flaring atmosphere (top source) than in the chromospheric levels at footpoints.

3.3.3. Comparison of the simulated HXR emission spectra with the RHESSI observations

We have analyzed the spectral observations of two flares: 20th July, 2002 and 23rd July, 2002 observed with RHESSI. The spectra for the first flare were produced by ourselves, while for the second flare they were produced by Holman et al. (2003). The spectra for both flares clearly reveal a low-energy flattening that appears during the rising phase of the flares (Fig. 13) similar to those caused by the return current effect (see Sect. 3.3.1).

For the analysis of the flare of 23 July 2002 we used the RHESSI photon spectra obtained for the times 00:23:44 UT and 00:25:32 UT (Holman et al. 2003) presented on panels a) and b) in Fig. 14, respectively. The high-energy spectral indices were found to be about 6.2 for both times, corresponding to an initial beam spectral index of about ~4.7. The observed low-energy indices are 5.2 at the first time and 4.8 at the second time. These photon spectral indices can be produced by a single electron beam simulation with spectral index 4.7 but with an increased initial energy flux, from $\sim 1 \times 10^9$ at 00:23:44 UT to $\sim 4 \times 10^9$ erg cm^{-2} s^{-1} at 00:25:32 UT. The break energy in both observed spectra was about 30–35 keV, which is also in good agreement with those in the simulated spectra for a single precipitating beam with the given parameters.

The estimations of the theoretical photon spectra and the analysis of the light-curves of the flare of July 23, 2002 allows us to suggest a simplified form for the initial flux temporal variations:

$$F_0(t) = 10^7 \mathrm{e}^{0.0256\,t(s)} \left(\mathrm{erg\ cm^{-2}\ s^{-1}}\right),\ \text{if } t < 360 \text{ s},$$

$$F_0(t) = -10^7 \mathrm{e}^{0.0256\,(t(s)-720)} \left(\mathrm{erg\ cm^{-2}\ s^{-1}}\right),\ \text{if } t < 360 \text{ s},$$

where t is the time after 00:21:00 UT.

The total bremsstrahlung intensity from 1 cm^2 of the flare area, I_{tot}, integrated over photon energy, was calculated using the initial beam distribution functions with the fitted beam parameters for an energy range of 16−160 keV. The intensity was found to be $I_{\mathrm{tot}} = 9.1 \times 10^6$ cm^{-2} s^{-1} at 00:23:44 UT and $I_{\mathrm{tot}} = 2.8 \times 10^7$ cm^{-2} s^{-1} at 00:25:32 UT. The visible area of this flare was about 49 sq. arcsec, which corresponds to $\sim 2.5 \times 10^{17}$ cm^2. The position of the flare was 72E and 13S, hence, taking the projection effect into account, an actual area of the flare is equal to 8.9×10^{17} cm^2. Using these parameters, one can calculate the photon count flux from the flare near the Earth as $F_{\mathrm{tot}} = \frac{S_{\mathrm{real}}}{4\pi L_{\oplus\odot}^2} \cdot I_{\mathrm{tot}}$ (here $L_{\oplus\odot}$ means distance from the Sun to the Earth). This photon flux F_{tot} was found to be 2.9×10^3 cm^{-2} s^{-1} and $\approx 8.9 \times 10^3$ cm^{-2} s^{-1} at 00:23:44 UT and 00:25:32 UT, respectively, which corresponds to the order of magnitude of the photon fluxes integrated from the observational light curves ($\sim 8 \times 10^3$ and $\sim 3 \times 10^4$ cm^{-2} s^{-1} for the first and second times). This confirms the estimations above of the initial energy flux for beam electrons that are assumed to be responsible for the production of the broken power-law HXR photon spectra. In addition, a single beam with such an initial flux and with the spectral index of about 4.5–5.0 can explain the temporal variations of the HXR spectra in this flare.

The spectra of the flare July 20, 2002 taken for the times 21:15:20 UT and 21:20:20 UT (Figs. 13c and d) were analysed using the same procedure. The photon spectra observed from this flare were harder than those for the July 23 flare with higher energy spectral indices, which were equal to 5.5 and 6.0 for these two times, respectively. This corresponded to initial beam spectral indices of 4.1 and 4.6. The lower energy spectral photon indices were equal to 3.5 and 3.0, which fits well with those produced by a single electron beam with spectral index 4.1 and initial energy flux about $\sim 3 \times 10^{10}$ erg cm^{-2} s^{-1} for the first time and spectral index 4.6 and energy flux of $\sim 5 \times 10^{10}$ erg cm^{-2} s^{-1} for the second one.

Therefore, the inclusion of Ohmic heating into the kinetic problem gives a reasonable explanation of the elbow-type structure in the HXR photon spectra caused by the precipitation of a single electron beam. Ohmic energy losses in addition to collisions lead to faster diffusion of beam electrons to lower energies which results in the noticeable flattening of their resulting photon spectra at energies below 50 keV.

4. Conclusions

In the current paper we present numerical solutions of the time-dependent kinetic Fokker-Planck equation for fast electrons injected into a flaring atmosphere from the corona that precipitate with energy and pitch-angle diffusion into a loop with a converging magnetic field. The electrons are assumed to lose their energy in Coulomb collisions with particles of the partially ionised ambient plasma and in Ohmic heating owing to the electric field induced by the precipitating beam. The energy and pitch-angle distributions of precipitating and return current electron beams at the various atmospheric column densities are presented as well as the precipitating beam densities, energy fluxes and resulting hard X-ray bremsstrahlung (photon) spectra for energy power law electron beams with spectral indices of 3, 5, 7 and initial energy fluxes of 10^8, 10^{10}, 10^{12} erg cm^{-2} s^{-1}.

Electron distribution functions, electron flux and hard X-ray spectra are found to be strongly dependent on the mechanisms taken into account for the kinetic analysis. The depth variations of the beam electron distribution functions are strongly affected by energy diffusion owing to collisions with charged (corona and TR) and neutral particles (chromosphere) of the ambient plasma. The collisional energy diffusion results in a shift to lower energies of the initial beam electron

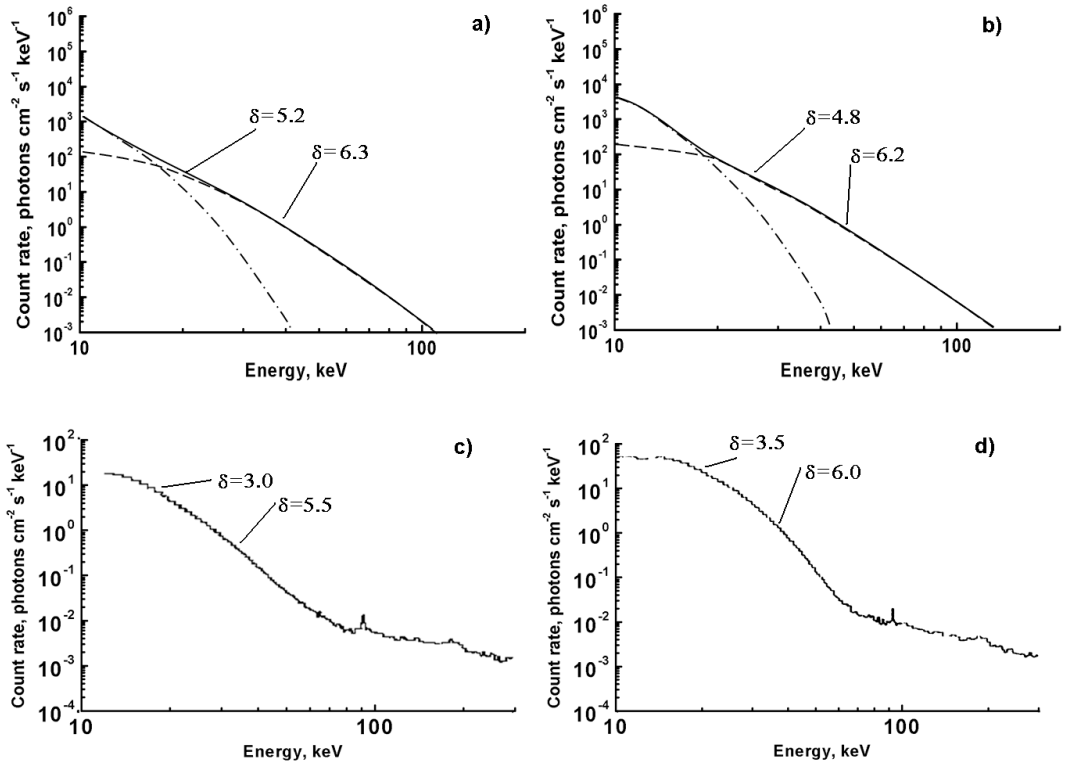

Fig. 13. Low-energy flattening in the non-thermal bremsstrahlung spectra observed with RHESSI in the flares of 23 (**a**), **b**)) and 20 (**c**), **d**)) of July, 2002. HXR spectra observed in the 23 July flare at 00:23:44 UT **a)** and 00:25:32 UT **b)** (the courtesy of Holman et al. 2003) were fitted by the HXR simulations produced by a beam with initial electron spectral index $\gamma = 3.7$ and with initial energy flux $\sim 3 \times 10^9$ erg cm^{-2} s^{-1} at the first moment and $\sim 10^{10}$ erg cm^{-2} s^{-1} at the second one. The plots **c)** and **d)** present the HXR spectra for the flare of 20th of July, 2002 taken at 21:15:20 UT and 21:20:20 UT respectively, which were also fitted by a single beam simulation (see for details Sect. 3.3.3).

energies resulting in a gradual decrease of the lower and upper energy cut-offs ($E_{\rm low}, E_{\rm upp}$) with depth. This energy shift also appears in the electron power-law energy spectrum, which becomes flatter at the lower energy part because the low energy electrons deposit their energy more effectively, and are replaced by electrons with initially higher energies, but whose number is much lower because of the initial energy power-law distributions (see Sect. 3.1.1 and Fig. 1c).

Pitch-angle diffusion for a mono-energetic beam is reflected in a much steeper decrease in number than what is expected from energy diffusion only (see Sect. 3.1.2). Apparently, this happens because the beam electrons, which lose their energy in Coulomb scattering, are also scattered many times not only forward ($\mu > 0$) but backward ($\mu < 0$). Pitch-angle diffusion is effective for electrons at any energy while being stronger for lower-energy ones. The diffusion results in the electrons losing their energy faster and dissipating at higher atmospheric levels than the electrons propagating without pitch-angle scattering.

During electron precipitation from the corona to the chromospheric the ambient plasma ionisation degree decreases with the electron precipitation depth by 2 or 3 orders of magnitude, which reduces the effect of Coulomb energy losses in favour of collisions with neutral atoms with much lower scattering cross-sections. This leads to smaller energy losses by beam electrons and to their precipitation to much lower chromospheric levels.

The converging magnetic field does not strongly affect the beam electron energy losses but it is effective in pitch-angle scattering of beam electrons. Magnetic field convergence is found to cause beam electron trapping in the upper coronal levels and a substantial reduction of the number of precipitating electrons. This results in an increase of the coronal-to-chromospheric emission ratio nearly proportional to the magnetic field convergence, but saturating after it exceeds 40. However, at the lower chromospheric levels in a weakly ionised plasma where the main channels of energy loss are collisions with neutrals, a converging magnetic field helps to collimate the precipitating beams, allowing some electron beams to penetrate to deeper chromospheric levels, even to the photosphere.

The effect of the electric field induced by a precipitating electron beam appears as an additional electron beam moving in the opposite direction back to the coronal source, or a return current with a nearly isotropic pitch angle distribution. The depths at which the return current is significant depend on the precipitating beam parameters; i.e. the return current for softer and weaker beams extends between the injection point and the lower corona, while for harder and more intense beams it reaches the transition region or upper chromosphere. The maximum energy of the return current is limited to less than 90 keV for harder and weaker beams, decreasing to 70 keV for softer and moderate beams or even to 60 keV for more intense

and soft beams. The return current energy distributions resemble exponential ones with maxima shifting towards higher energy for harder and more intense beams. This is likely to be caused by a combination of much more effective pitch-angle and energy diffusion for lower-energy than for higher-energy electrons, leading to a maximum in the returning electron number that depends on the depth at which the return current is formed. Hence, for a given value of direct beam spectral index, the same fraction of all beam particles will either mirror or undergo pitch-angle diffusion taking them in the reverse direction. So, in order to neutralise a more intense beam, a higher absolute number of particles has to be accelerated by the electric field out of the ambient plasma. These particles will have a lower energy than the typical mirroring particles, so the overall energy distribution for the return current associated with a less intense beam is narrower than that for a more intense beam.

As a result, the photon spectra of hard X-ray emission emitted from a flaring atmosphere are found to have broken power-law spectra with the higher energy part retaining the spectral index $\delta_{\rm high}$ associated with the electron beam's initial index γ that increases as $\delta = \gamma + A$, where $A = 1.5$–2.0. The lower energy part of the X-ray photon spectra reveals a much smaller increase or even a substantial decrease of its spectral index $\delta_{\rm low}$, i.e. $A < 0$.

The simulated broken power-law photon spectra produced by precipitating electron beams with a single spectral index and initial energy fluxes agree well with photon energy spectra observed by RHESSI from the 20th and 23rd July, 2002 flares. Both higher- and lower-energy spectral indices deduced from simulations are in good agreement with those observed. The break energy in both observed spectra was about 30–35 keV, which is also in good agreement with those in the simulated spectra for a single precipitating beam with the given parameters.

Therefore, the kinetic effects taking into account energy and pitch-angle diffusion, non-uniform ionisation, converging magnetic and induced electric field are essential for a description of the electron beam precipitation into a flaring atmosphere and its resulting hard X-ray spectra. These effects can explain many essential features in the observed photon spectra like the total energy emitted in the flare as bremsstrahlung, its broken power-law spectra that can also be very easily compared with the restored electron spectra obtained by various inversion methods. This approach can also be useful for the interpretation of temporal variations of hard X-ray and UV emission from a flaring atmosphere if the atmospheric heating by beam electrons is taken into account. This will be the subject of a forthcoming paper.

Acknowledgements. This research has been supported by the Engineering and Physical Sciences Research Council (UK), grant GR/R53449/0. The authors would like to express their deepest gratitude to the anonymous referee for his very detailed and constructive comments from which the paper has strongly benefited. Also the authors would like to thank Dr. John Baruch for his useful comments and discussion of the paper.

References

Benka, S. G., & Holman, G. D. 1992, ApJ, 391, 854
Benz, A. O. 2002, Plasma Astrophysics: Kinetic Processes in Solar and Stellar Coronae (Kluwer Acad. Publ.)
Birdsall, Ch. K., & Langdon, A. B. 1985, Plasma Physics via Computer Simulation (McGraw-Hill Book)
Brown, J. C. 1971, Sol. Phys., 18, 489
Brown, J. C. 1972, Sol. Phys., 25, 158
Conway, A. J., Brown, J. C., Eves, B. A. C., & Kontar, E. 2003, A&A, 407, 725
Diakonov, D. V., & Somov, B. V. 1988, Sol. Phys., 116, 119
Elwert, G., & Haug, E. 1970, Sol. Phys., 15, 234
Emslie, A. G. 1978, ApJ, 224, 241
Emslie, A. G. 1980, ApJ, 235, 1055
Fletcher, L. 1996, A&A, 310, 661
Fletcher, L., & Hudson, H. S. 2002, Sol. Phys., 210, 307
Gordovskyy, M., & Zharkova, V. V. 2003, Proc. PREP-2004 Conference, ed. A. O'Neil, University of Exeter, 187
Holman, G. D., & Benka, S. G. 1992, ApJ, 400, 79
Holman, G. D., Sui, L., Schwartz, R. A., & Emslie, A. G. 2003, ApJ, 595, L97
Knight, J. W., & Sturrock, P. A. 1977, ApJ, 318, 206
Kontar, E. P., Brown, J. C., & McArthur, G. K. 2002, Sol. Phys., 210, 419
Kontar, E. P., Brown, J. C., Emslie, A. G., et al. 2003, ApJ, 595, L123
Krall, N. A., & Trivelpiece, A. W. 1973, Principles of Plasma Physics (Tokyo: McGraw-Hill)
Kundu, M. R. 1984, Sol. Phys., 100, 491
Landau, L. D. 1937, Zhurn. Experim. Theor. Phys, 7, 203
Leach, J., & Petrosian, V. 1981, ApJ, 142, 241
Leach, J., & Petrosian, V. 1983, ApJ, 279, L715
Lin, R., Mewaldt, R. A., & van Hollebeke, M. A. I. 1982, ApJ, 253, 949
Lin, R., Krucker, S., Hurford, G. J., et al. 2003, ApJ, 595, L69
Mauas, P. J. D., & Gomez, D. O. 1997, ApJ, 483, 496
McClements, K. G. 1990, A&A, 234, 487
McClements, K. G. 1992a, A&A, 253, 261
McClements, K. G. 1992b, A&A, 258, 542
McKinnon, A. L., & Craig, I. J. D. 1991, A&A, 251, 693
Nocera, L., Skrynnikov, Yu. I., & Somov, B. V. 1985, Sol. Phys., 97, 81
Seaton, D. B., Winebarger, A. R., DeLuca, E. E., et al. 2001, ApJ, 563, L173
Shapiro, P. R., & Knight, J. W. 1978, ApJ, 224, 1028
Sui, L., Holman, G. D., Dennis, B. R., et al. 2002, Sol. Phys., 210, 245
Syniavskii, D. V., & Zharkova, V. V. 1994, ApJS, 90, 729
Syrovatskii, S. I. 1968, Ionization Losses (Moscow: Nauka) (in Russian)
Syrovatskii, S. I., & Shmeleva, O. P. 1972, AZh, 49, 334
Tindo, I. P., Ivanov, V. D., Mandelshtam, S. L., & Shurygin, A. I. 1972, Sol. Phys., 24, 429
Vilmer, N., Krucker, S., Lin, R. P., & RHESSI team 2002, Sol. Phys., 210, 261
Willson, R. F., & Holman, G. D. 2003, AAS SPD meeting, 34, 1620
Zharkova, V. V., & Kobylinskii, V. A. 1993, Sol. Phys., 143, 259
Zharkova, V. V., Brown, J. C., & Syniavskii, D. V. 1995, A&A, 304, 284
Zhitnik, I. A., Urnov, A. M., Zharkova, V. V., & Ivanchuk, V. I. 1993, Preprint of the Lebedev Physics Institute, Moscow, 45

Online Material

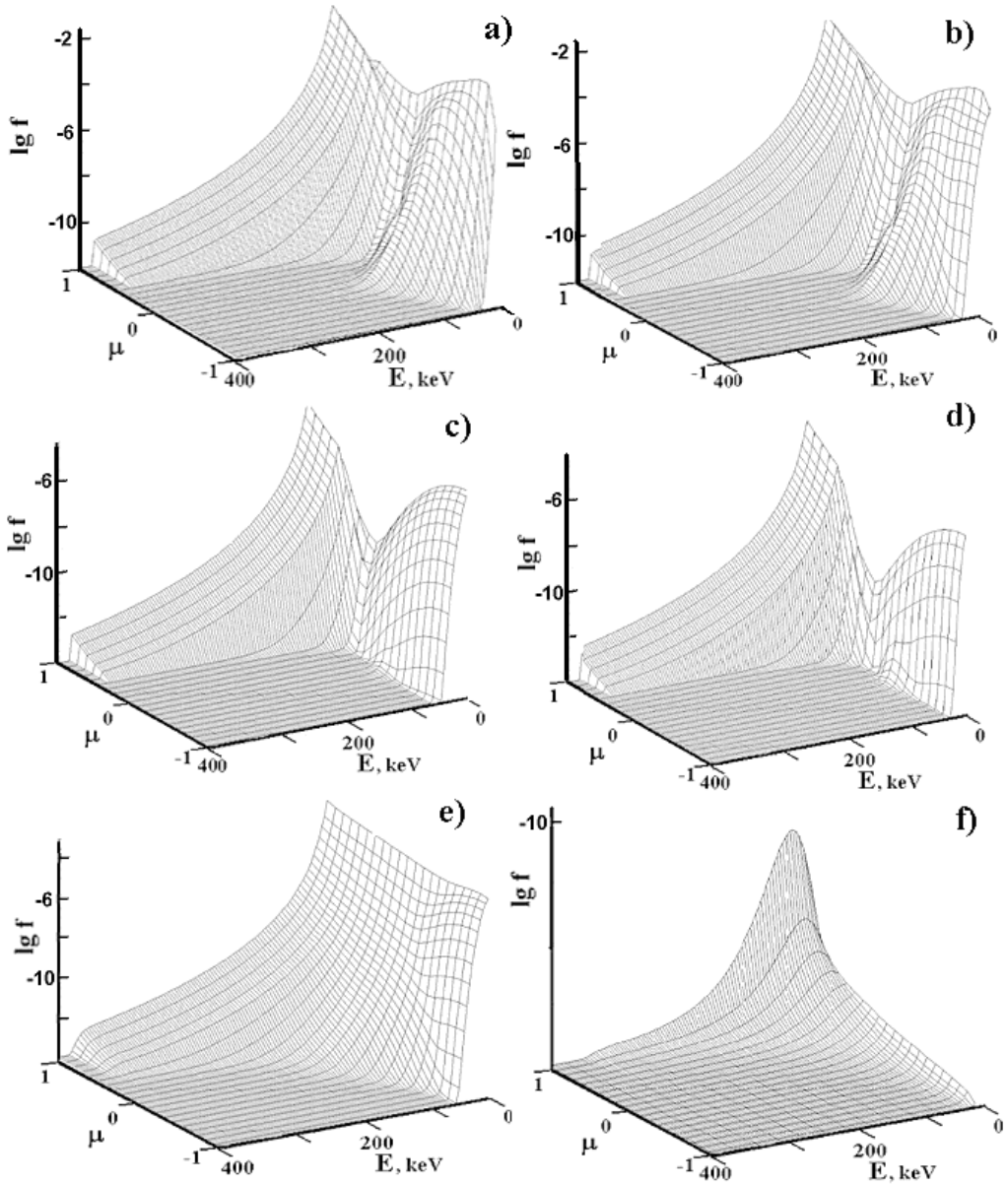

Fig. 3. Energy – pitch-angle ($E-\mu$) distributions (vertical axis) versus energy E and pitch-angle cosines μ calculated with a return current effect for a beam injected with the energy range 16−384 keV, spectral index $\gamma = 3$ and initial energy flux 10^{10} erg cm^{-2} s^{-1}. **a)** Corresponds to the column density 4.2×10^{17} cm^{-2}; **b)** to 8.4×10^{17}; **c)** to 1.8×10^{18}; **d)** to 1.3×10^{19}; **e)** to 5.1×10^{20} and **f)** to 2.9×10^{22} cm^{-2}.

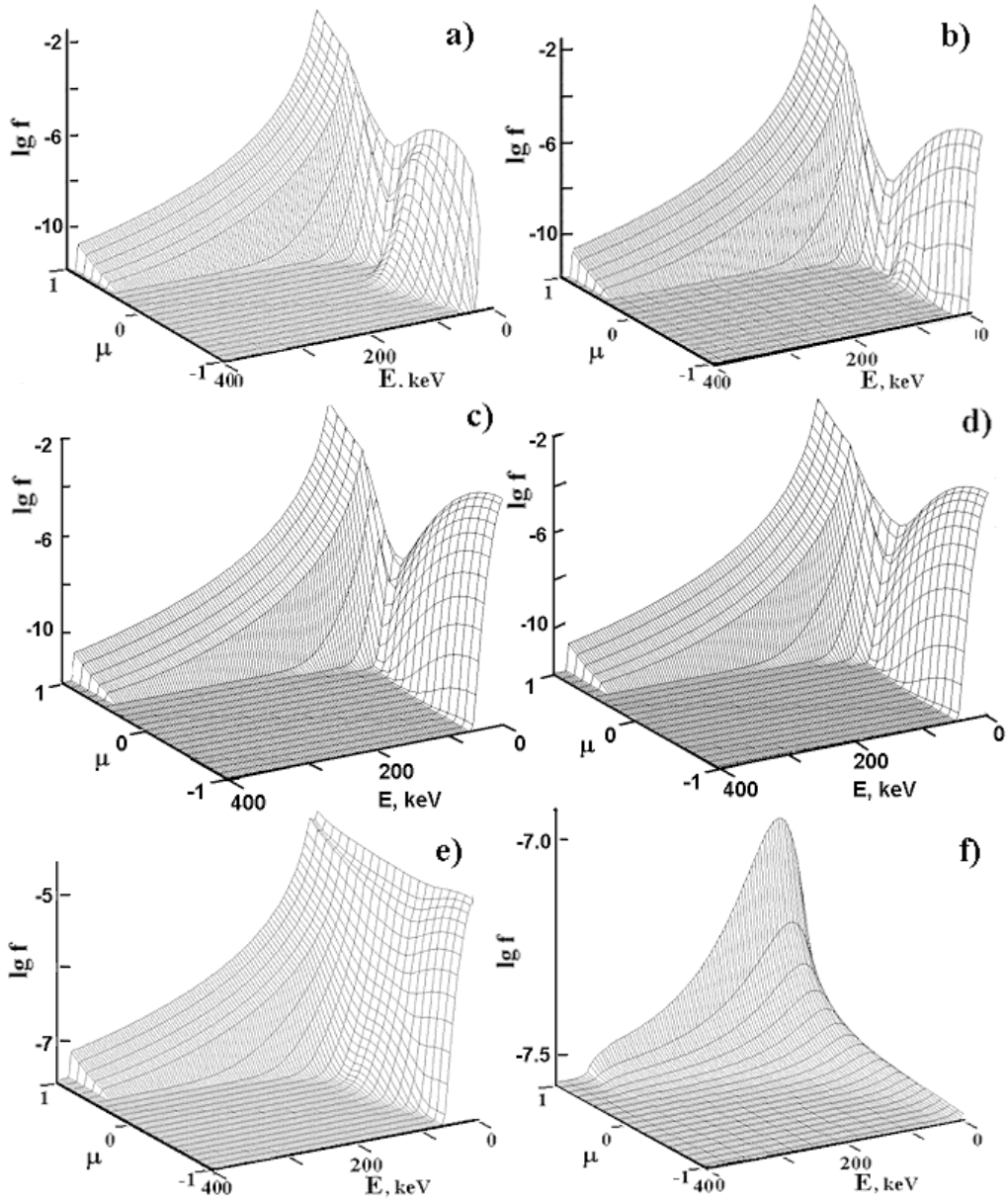

Fig. 4. The same as in Fig. 3 but for spectral index γ = 7 and initial energy flux 10^{10}.

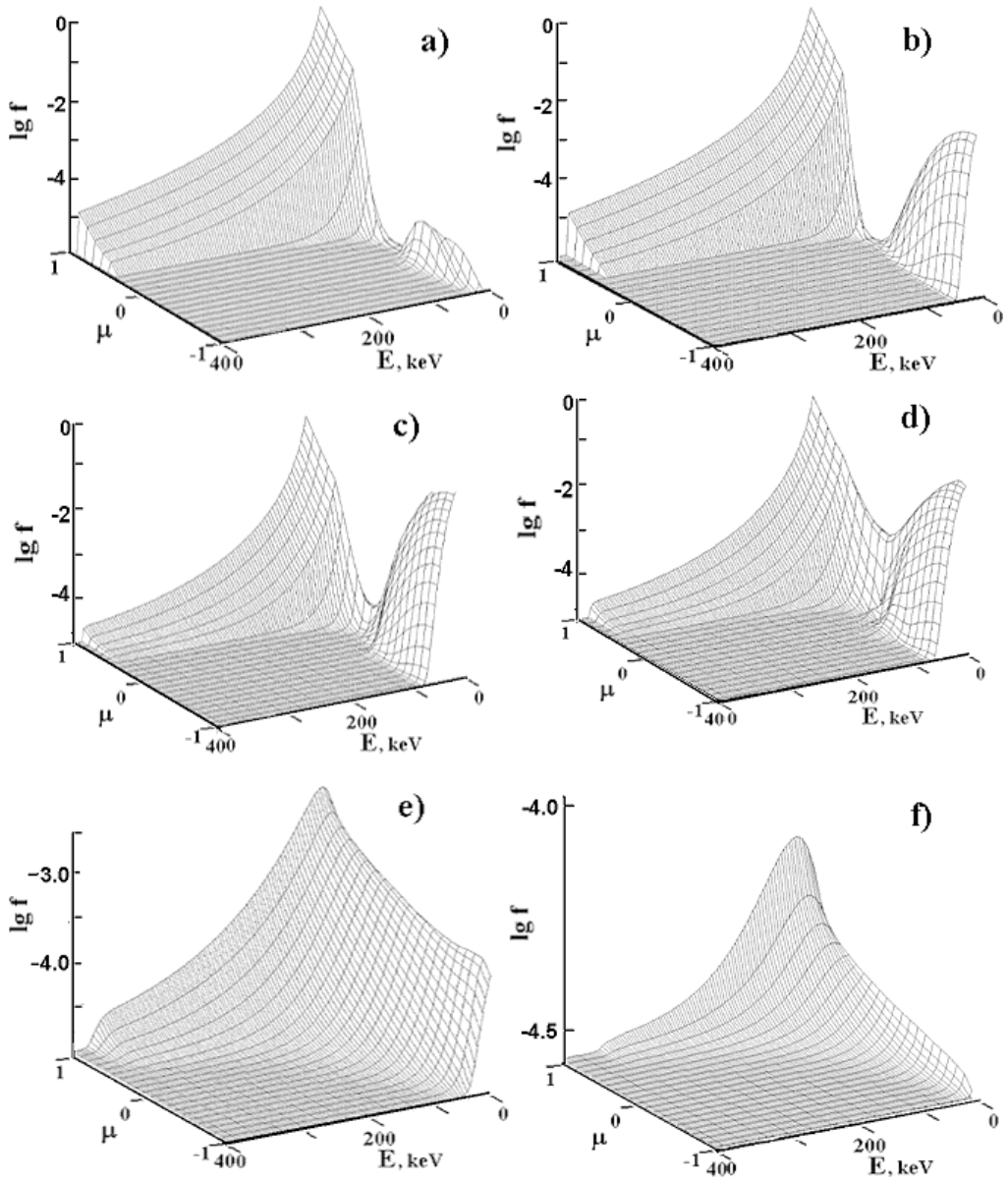

Fig. 5. The same as in Fig. 3 but for spectral index $\gamma = 3$ and initial energy flux 10^{12}.

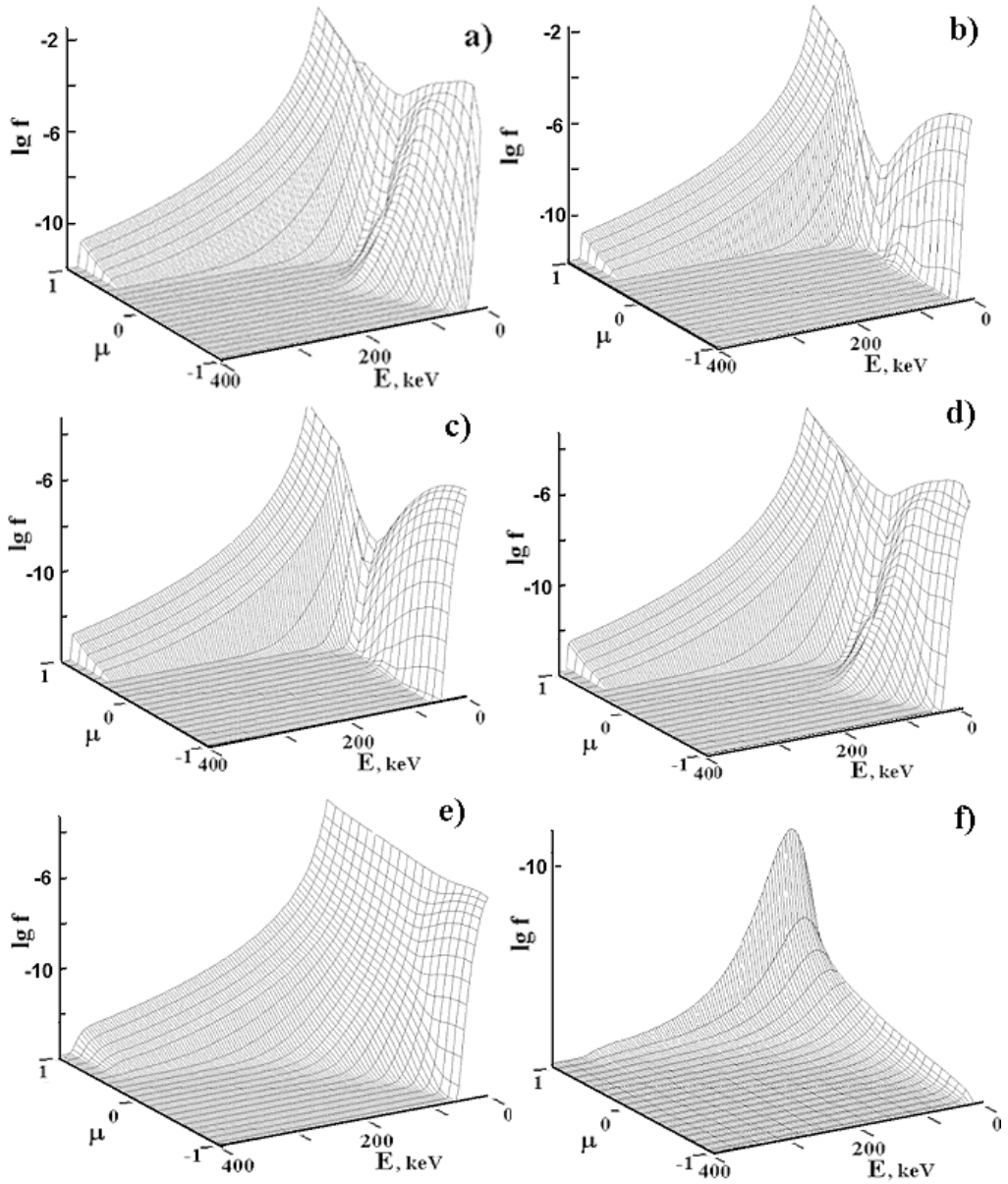

Fig. 6. The same as in Fig. 3 but for spectral index $\gamma = 7$ and initial energy flux 10^{12}.